TRIMETALIC HETEROGENEOUS CATALYST FOR DEHYDROGENATION OF FORMIC ACID WITH ENHANCED CO TOLERANCE

A THESIS SUBMITTED TO
THE GRADUATE SCHOOL OF ENGINEERING AND SCIENCE
OF BILKENT UNIVERSITY
IN PARTIAL FULFILLMENT OF THE REQUIREMENTS FOR
THE DEGREE OF
MASTER OF SCIENCE
IN
CHEMISTRY

By
Elif Perşembe
September 2017

TRIMETALIC HETEROGENEOUS CATALYST FOR DEHYDROGENATION OF FORMIC ACID WITH ENHANCED CO TOLERANCE

By Elif Perşembe

September 2017

We certify that we have read this thesis and that in our opinion it is fully adequate, in scope and in quality, as a thesis for the degree of Master of Science.

_____

Emrah Özensoy (Advisor)

_____

Mehmet Zahmakıran

_____

Ömer Dağ

Approved for the Graduate School of Engineering and Science:

_____

Ezhan Karaşan
Director of the Graduate School

ABSTRACT

TRIMETALIC HETEROGENEOUS CATALYST FOR DEHYDROGENATION OF FORMIC ACID WITH ENHANCED CO TOLERANCE

Elif Perşembe

M.S. in Chemistry

Supervisor: Emrah Özensoy

September, 2017

Hydrogen energy is considered to be a promising alternative for the sustainable and environmentally friendly solution of the global energy problem. One of the major obstacles of hydrogen energy applications is to maintain safe and efficient storage of hydrogen which can also be achieved chemically using suitable carrier materials. Formic acid (HCOOH, FA) can be utilized as a hydrogen carrier due to its low molecular weight (46 g/mol) and high hydrogen density (%4.4 weight). FA is a stable, non-flammable, and non-toxic biomass side-product rendering it a perfect candidate for an alternative hydrogen vector. Design of novel heterogeneous catalysts which can substitute the existing homogeneous catalytic systems may allow overcoming catalyst isolation and recovery costs and associated logistical problems hindering their applications in on-board operations.

FA can be catalytically decomposed via dehydrogenation and dehydration reactions. Selective dehydrogenation of FA is crucial because, the production of CO from dehydration mechanism can suppress the activity of the catalyst by blocking/poisoning the precious metal sites. Consequently, development of CO-resistant, selective, catalytically active, and reusable heterogeneous catalysts has a great significance. In the current work, a new material that can produce H_2(g) from FA

under ambient conditions in the absence of additives with high CO-poisoning tolerance will be introduced, which is comprised of Pd-based trimetallic active centers functionalized with Ag and Cr in addition to amine-functionalized MnO_x promoters dispersed on a SiO_2 support surface.

A novel trimetallic FA dehydrogenation catalyst was prepared and studied using analytical, ex-situ and in-situ spectroscopic techniques and compared to the results obtained for monometallic, bimetallic and active site-free counterparts. Trimetallic catalysts were found to reveal superior catalytic activity and stability compared to all of the currently investigated catalysts. Structural and catalytic properties of the trimetallic catalysts were investigated as a function of metal loadings. Structural characterization of the synthesized materials was carried out by Raman spectroscopy, Inductively-Coupled Plasma Optical Emission Spectroscopy (ICP-OES), X-ray Diffraction (XRD), Brunauer, Emmett and Teller (BET) Specific Surface Area Analysis, Transmission Electron Microscopy (TEM), High Resolution TEM (HRTEM), Scanning Transmission Electron Microscopy (STEM), and STEM/Energy Dispersive X-Ray (EDX), High-Angle Annular Dark Field (HAADF)/STEM. In addition, interaction of the catalyst surfaces with reactants and products were also monitored *via in-situ* FTIR spectroscopy for functional characterization. Detailed *in-situ* FTIR spectroscopic experiments were also performed using HCOOD, DCOOH and DCOOD in order to understand the nature of the adsorbed species, products and catalytic inhibitors.

Keywords**:** Hydrogen, Formic Acid, Dehydrogenation, Manganese, Palladium, Silver, Chromium, Alloy, Isotopic Labelling, Heterogeneous Catalyst.

ÖZET

FORMİK ASİT DEHİDROJENLEME TEPKİMESİ İÇİN
YÜKSEK KARBON MONOKSİT DİRENCİNE SAHİP
ÜÇ-METALLİ HETEROJEN KATALİZÖRLER

Elif Perşembe
Kimya, Yüksek Lisans
Tez Danışmanı: Emrah Özensoy
Eylül, 2017

Hidrojen enerjisi teknolojileri, küresel enerji problemine sürdürülebilir ve çevre dostu çözümler vaad eden alternatif yaklaşımlar olarak görülmektedir. Hidrojen enerji süreçlerinin uygulanabilirliğinin önüne geçen en büyük engel; güvenli ve verimli hidrojen depolama sistemlerinin eksikliğidir. Bu anlamda, hidrojenin kimyasal olarak uygun taşıyıcılarda depolanması, yüksek basınçlı fiziksel depolama yöntemine göre daha güvenlidir. Formik asit (FA) düşük moleküler ağırlığı (46 g/mol), yüksek hidrojen yoğunluğu (%4.4 weight) ve uygun fiziksel/kimyasal özellikleri sebebiyle, hidrojen taşıyıcısı olarak yüksek bir potansiyele sahiptir. Yapısal kararlılığının yanında, zehirli veya yanıcı olmaması, FA'i alternatif bir kimyasal taşıyıcı olarak çok daha öne çıkartmaktadır. FA'den hidrojen üretimi için heterojen katalizörlerin kullanımı, homojen katalizörlerin kullanıldığı konvansiyonel sistemlerdeki, katalizör izolasyonu ve geri kazanımına dair teknik zorluklar ve ek maliyetleri ortadan kaldırma olasılığını taşımaktadır.

FA katalik olarak dehidrojenlenme ve dehidrasyon tepkimeleri ile parçalanabilir. FA'nın seçici dehidrojenlenme tepkimesi, alternatif bir tepkime olan ve parallel olarak gerçekleşen, dehidrasyon tepkimesi sonucu oluşan CO (g)'nun aktif

noktaları zehirlemesi sebebiyle baskılanabilmektedir. Dehidrasyon yoluyla oluşan CO (g), değerli metal üzerine yapışarak aktif alanları kolayca bloke edebilmektedir. Dolayısıyla, CO'ya dayanıklı, seçici, katalitik olarak aktif ve tekrar kullanılabilir, uzun ömürlü heterojen bir katalizörün sentezi büyük önem taşımaktadır. Bu güncel çalışmada, katkı maddesine ihtiyac duymadan, ılımlı koşullarda, FA'ten H_2 (g) üreten, CO zehirlenme direnci yüksek, yeni bir heterojen katalizör sunulmuştur. Bu yeni malzeme, üç-metalli aktif noktların, amin grupları ile işlevselleştirilmiş MnO_x ile katkılandırılması ve SiO_2 taban malzemesi üzerine dağıtılmasıyla elde edilmiştir.

Bu özgün üç-metalli FA dehidrojenleme katalizörünün sentezi ve karakterizasyonu; tek metalli, iki metallic ve hiç metal içermeyen türevleriyle karşılaştırmalı olarak incelenmiştir. Üç metalli katalizörün incelenen diğer tüm katalizöre kıyasla, daha üstün aktivite gösterdiği saptanmıştır. Yüksek verilmlilik ile çalışan bu katalizörün yapısal ve katalitik özellikleri, ICP-OES ile takip edilen, farklı miktarlarda metal yüklemeleri yapılarak incelenmiştir. Sentezlenen malzemelerin yapısal karaterizasyonu, Raman spektroskopisi, XRD, BET, TEM, HRTEM, STEM ve STEM/EDX, HAADF/STEM gibi tekniklerle incelenmiştir. İşlevsel karaterizasyon deneylerinde, tepkimeye girenlerin ve ürünlerin katalizör yüzeyi ile etkileşimi, *in-situ* FTIR tekniği ile çalışılmıştır. Adsorblanan türler, ürünler ve katalitik inhbitörler, hidrojen izotopu olan döteryum ile etiketlenmiş, HCOOD, DCOOH ve DCOOD kullanılarak, *in-situ* FTIR tekniğiyle, ayrıntılı şekilde incelenmiştir.

***Anahtar kelimeler*:** Hidrojen Üretimi, Formik Asit, Dehidrojenleme, Mangan, Paladyum, Gümüş, Krom, Alaşım, İzotop Etiketleme, Heterojen Katalizör.

ACKNOWLEDGEMENT

I would like to thank Assoc. Prof. Emrah Özensoy for his admirable enthusiasm for teaching and guidance through my studies. I am very grateful for the opportunity he gave me. I am truly honored to be in his research group and be taught by him.

I would also like to thank Assoc. Prof. Mehmet Zahmakıran and his group for their collaboration and very valuable contributions to this study. I would like to thank my jury members Prof. Ömer Dağ and Assoc. Prof. Mehmet Zahmakıran. Special thanks to Specs GmbH for their help in XPS measurements

I acknowledge TÜBİTAK for financial support (Project Code:115Z552).

I would like to thank to all Özensoy group members, especially to Merve Kurt, Kerem Ercan, and Mustafa Karatok for their support and cooperativeness. I am sincerely grateful to Zafer Say for his precious advices both in academic and personal life.

I am very grateful to have Menekşe Liman as a friend who has always been supportive in every possible way. I could not stay chill without her emotional support.

I have a great appreciation for Tuluhan Olcayto Çolak for being the best friend one can ever have. His endless but pleasant conversations will always be remembered. His companionship in late night studies was very encouraging.

I feel very fortunate to have Emel Balkan in my life. Her kindness, understanding and warm heart shaped my character throughout the years. I could never get rid of my flaws if she wasn't nourishing. She is the one I try to become and will always be my heroine.

Special thanks to Dad for guiding me through this discipline in my early ages. His exceptional passion for science created my first drive for chemistry. Dad’s and Mom’s support had been very encouraging in my studies. I can never express how grateful I am for having such a family with high moral and ethical values.

I also would like to express my gratitude to Furkan who has always been open and trustworthy. His attitude to stay true always fascinated me and affected me in the best way.

My greatest appreciation is for my dear partner whom I cherish the most. He supported me unconditionally in every imaginable way, bared with me when was tough. I found peace in his calmness and freedom in his arms. He always believed in me, respected to the choices I made and gave me the strength to beat the struggles of life. I could never imagine someone giving so much comfort and independence at the same time. I am very happy to have him in my life, in our journey.

Dedicated to Mustafa Babil

LIST OF ABBREVIATIONS

APTS	3-Aminopropyltriethoxysilane
BET	Brunauer-Emmett-Teller
EDX	Energy-Dispersive X-ray spectroscopy
FA	Formic Acid
FTIR	Fourier Transform Infrared Spectroscopy
HAADF	High-Angle Annular Dark Field
PEMFC	Proton Exchange Membrane Fuel Cells
ICP-OES	Inductively Coupled Plasma Optical Emission Spectrometry
IR	Infrared
JCPDS	Joint Committee on Powder Diffraction Standards
NIST	National Institute of Standards and Technology
PID	Proportional Integral Derivative
QMS	Quadruple Mass Spectrometer
SEM	Scanning Electron Microscopy
SSA	Specific Surface Area
STEM	Scanning Transmission Electron Microscopy
TEM	Transmission Electron Microscopy
TPD	Temperature Programmed Desorption
XRD	X-Ray Diffraction

TABLE OF CONTENTS

LIST OF FIGURES

LIST OF TABLES

CHAPTER 1

INTRODUCTION

1.1. Practical Needs for Alternative Fuels

Fossil fuels like petroleum, natural gas, and coal are natural feedstocks which are currently being used to satisfy the majority of the global energy demand. However these natural resources are consumed rapidly, and the pollutants resulting from the combustion of these fossil fuels lead to greenhouse effect, ozone depletion, acid rains and a multitude of risks for the human health [14], [15]. Thus, there is an immediate need for alternative fuels to circumvent the industrial, economic and environmental drawbacks associated with fossil fuel utilization. One of the most promising solutions in this respect is the construction of the 'Hydrogen Economy' corresponding to an industrial system using hydrogen as the primary energy carrier [16]. The high specific energy of hydrogen (33.3 kWh/kg) which is significantly higher than most of the conventional fossil fuels makes it a very powerful candidate as an alternative fuel [1].

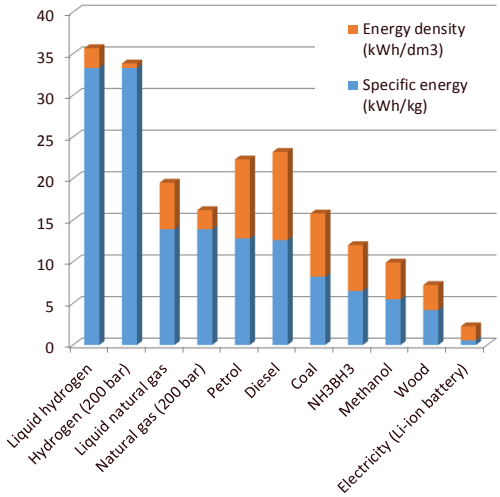

Fuel	Specific energy (kWh/kg)	Energy density (kWh/dm³)
Liquid hydrogen	33.3	2.37
Hydrogen (200 bar)	33.3	0.53
Liquid natural gas	13.9	5.6
Natural gas (200 bar)	13.9	2.3
Petrol	12.8	9.5
Diesel	12.6	10.6
Coal	8.2	7.6
NH_3BH_3	6.5	5.5
Methanol	5.5	4.4
Wood	4.2	3.0
Electricity (Li-ion battery)	0.55	1.69

Figure 1. Comparison of Specific energy (kWh/kg) and energy density (kWh/dm^3) of various types of fuels [1] (Copyright © Elsevier, 2008).

Hydrogen is an odorless, colorless, tasteless and most importantly a non-poisonous gas allowing easy and clean production whose utilization results in almost zero pollutants [16]. A very drastic shift from the existing energy production, distribution and utilization infrastructures is required to switch to the hydrogen economy. Mechanical storage of H_2 for fuel cell applications is both technically and financially challenging since it needs to be stored either under high pressure or in liquid tanks (due to the need for the high energy density per volume) [1], [17], [18].

Hydrogen can be used to generate electricity through fuel cells [14]. Different types of fuel cells exist which are entitled categorized based on the electrolyte used such as alkaline fuel cells (AFC), phosphoric acid fuel cells (PAFC), molten carbonate fuel cells (MCFC), solid oxide fuel cells (SOFC), and one of the most promising candidate for light duty vehicle applications; proton exchange membrane fuel cells (PEMFC) [14]. Direct PEMFC use ultra-pure hydrogen to operate requiring safe, light-weight, low-cost hydrogen storage media with fast and controlled release limiting their extensive usage [19]. Consequently, application employing indirect fuel cells where a chemical vector is used as the hydrogen carrier is becoming popular. Metal hydrides were considered as one of the promising hydrogen storage media, however their slow kinetics, high desorption temperatures and reversibility problems led to a search for new storage media which are easily produced and are also stable in liquid phase at room temperature [20], [21].

One of the outstanding chemical hydrogen storage materials is formic acid (HCOOH, FA) and there is a growing interest in FA dehydrogenation due to its desirable properties.

1.2. Formic Acid as a Hydrogen Carrier

Production of methanol and formic acid by reduction of carbon dioxide with molecular hydrogen is a sustainable and renewable way of energy utilization. Although methanol has higher hydrogen content by mass (*i.e.* 12.6 % w/w) with respect to that of FA (*i.e.* 4.4 % w/w), production of FA from carbon dioxide seems to be more beneficial. Formation of methanol (CH_3OH) requires 3 equivalents of hydrogen where water is formed as an unwanted side product from which hydrogen recovery is quite challenging (*Equation 1.1.1*). On the other hand, there are no side products in FA formation from the hydrogenation of carbon dioxide (*Equation 1.2.2*) [22].

$$CO_2 + 3H_2 \rightarrow CH_3OH + H_2O \quad (1.2.1)$$

$$CO_2 + H_2 \rightarrow HCOOH \quad (1.2.2)$$

Low flammability, non-toxicity, lightness, relatively high hydrogen content and high stability under ambient conditions in liquid phase allow FA to be applicable for portable use in fuel cell technology due to its easy storage, handling, transportation/distribution, and fast refill. Besides, FA is biodegradable, renewable, sustainable, and readily available rendering it as a promising contender [13].

FA can be synthesized from many methods including carbonylation of methanol, but most importantly it can be produced in a renewable fashion from biomass (glucose, cellulose, starch) in an environmentally friendly fashion. 1 mole of glucose can yield 6 moles of FA by hydrothermal oxidation [23].

The primary advantages of FA in on-board hydrogen production applications can be summarized as follows;

a) Exists in liquid phase under ambient conditions.
b) High hydrogen content (4.4% (w/w)).

c) Biodegradable

d) Obtainable from biomass conversion and in a renewable and sustainable fashion. Favorable physical properties: Non-flammable, non-toxic, highly stable, low molecular weight (46 g/mol).

1.3. Production of Hydrogen from FA

Consideration of FA as a hydrogen carrier has been initially proposed in 1960's. Albeit, some of the challenges still remain. FA can thermally decompose *via* two reaction pathways; dehydrogenation (*Equation 1.3.1*) and dehydration (*Equation 1.3.2*).

Reaction Pathways	ΔG^{o}_{298K}	ΔH^{o}_{298K}
$HCOOH\ (l) \longrightarrow H_2(g) + CO_2(g)$ (1.3.1)	-33.0 kJ/mol	+31.2 kJ/mol
$HCOOH\ (l) \longrightarrow H_2O(l) + CO(g)$ (1.3.2)	-13.0 kJ/mol	+28.4 kJ/mol

Table 1. Catalytic decomposition of FA *via* dehydrogenation and dehydration pathways along with their ΔG^{o} and ΔH^{o} values at 298 K [13].

Since standard Gibbs free energy values for both of those reactions are negative, both reaction channels may occur in a competing fashion during the decomposition of FA. In order to operate, PEMFCs require an extremely pure hydrogen feed. Thus, a selective and highly active catalyst is required in order to generate hydrogen from FA without producing detrimental amounts of CO(g) that can poison the catalyst and decrease the purity of the produced hydrogen. Very small amounts (less than 10 ppm) of CO (g) can reduce the activity of the precious metal catalysts [14].

In addition, production of CO_2 (g) from dehydrogenation reaction does not pose an environmental risk due to its recyclability. Furthermore in such operations,

transportation costs are lowered since the weight that the engine carries are scaled down [22].

Consequently, the development of CO-resistant, catalytically active, selective, long lasting, and reusable heterogeneous catalysts has a great importance.

1.4. A Brief Look at FA Dehydrogenation Catalysts

Noticeably high catalytic activity and selectivity for FA dehydrogenation can be accomplished by using homogeneous catalysts such as $[RuH_2(PPh_3)_3CO]$ [24], $Fe(BF_4)_2[P(CH_2CH_2PPh_2)_3]$ [25], $[Rh(cp^*)(bipy)(H_2O)](SO_4)$ [26], and $[Ru_2H(\mu\text{-}H)(\mu\text{-}CO)(CO)_2(\mu\text{-}dppm)_2]$ [27] [28]. Long and complex synthesis protocols required for homogeneous catalysts and the need for the utilization of additives and additional solvents are some of the critical disadvantages of the homogenous catalytic FA dehydrogenation approaches [29], [30]. Furthermore, low yields and complications in catalyst reusability indicate that use of homogeneous catalysts may not be the ideal approach for dehydrogenation of FA. This is particularly true for on-board applications and auxiliary power applications for portable devices (*e.g.* cell phones, laptops) imposing additional space limitations.

A comprehensive survey of the heterogeneous catalysts for dehydrogenation of FA shows that in many cases [2], [31]–[34] additives such as sodium formate (HCOONa), primary amines (NH_2R) and Lewis acids ($LiBF_4$) are needed to initiate the catalytic process and even the presence of such additives does not warrant high catalytic conversion and selectivity in some cases. Heterogeneous catalysts that can selectively catalyze FA dehydrogenation reaction without any additives are very few while their performances are typically lower compared to homogeneous catalysts. Such heterogeneous catalysts use Pd as the primary active metal in the form of alloys or core@shell nanostructures with other metals and metal oxide promoters.

The investigation of adsorption and decomposition mechanism of FA on alumina and silica support surfaces goes back to 1960s [35]–[37]. Numerous Ultra-High Vacuum (UHV) surface science studies regarding the activation of FA on model catalyst single crystal surfaces such as Pd(100) [38], Ni(111) [39], Ni(110) [10], Al(111) [40], Ru(001) [41], Pt(111) [42], Cu(110) [43]–[45], Cu/SiO_2 [46], Ag(111) [9], Mo(100) [47] are also available. In addition, high surface area powder catalysts containing numerous derivatives of C supported catalysts such as Pd/C [48], Pd/MSC30 [31], PdAu/C, PdAg/C [33], C-AuPd [29], C-AgPd [49], PdNiAg/C [50], AuAgPd/Grapene [51], Ag/N-rGO, PdAg/N-rGO [52] were also synthesized, characterized and activity measurements were conducted. Some of the most active metals were studied with different support materials such as Rh, Pt, Au/TiO_2 [53], Au/ZrO_2 [34], $Pd\text{-}CeO_2$ [54], Pd/SiO_2 [55], [56] while core-shell structures attracted attention as well; $Pd@SiO_2$ [56], Ag@Pd [6], Au@Pd/N-mrGO [30].

Yamashita et al. [2] examined the effect of different acidic and basic functional resins in the dehydrogenation reaction of FA. The activity of Pd/resin with weakly basic functional group $-N(Me)_2$ was very high compared to other functional groups as well as to the catalysts with other support materials having the same Pd loading. FTIR and kinetic isotope effect experiments showed that $-N(Me)_2$ groups act as promoters for O-H bond dissociation by extracting the acidic H atom in FA. This is followed by the β-hydride elimination in the generated formate species attached on Pd NPs. This may result in CO_2 production as well metal-hydride formation followed by the reaction of hydride with protonated $N(Me)_2$ (Figure 2). Au on ZrO_2 with NEt_3 functionalities and amine assisted reaction was also investigated by another group [34] in a similar approach.

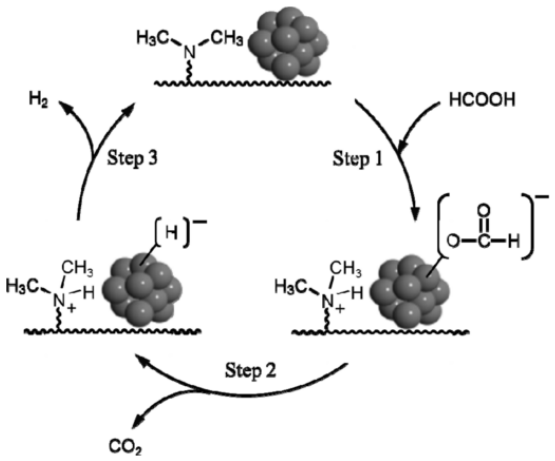

Figure 2. A possible FA decomposition mechanism with -N(Me)$_2$ functional group [2] (Copyright © American Chemical Society, 2013).

A new series of catalysts with Metal-MnO_x dispersed on amine grafted SiO_2 were designed by easy and reproducible synthesis protocols by Zahmakıran *et al.* Particularly, Pd-MnO_x/SiO_2-NH_2 [3], PdAu-MnO_x/SiO_2-NH_2 [57] and PdAg-MnO_x/SiO_2-NH_2 [12] catalysts were reported to be extremely active for additive-free FA dehydrogenation under mild conditions with high Turn Over Frequency (TOF), selectivity and conversion. The effect of -NH_2 functional groups on different support materials is summarized in Figure 3. The low activity of catalysts with C, TiO_2 and Al_2O_3 supports as well as amine-free SiO_2 can point out the significance of the amine functionalities along with the selection of the support material. Additionally, it is apparent that the amount of the -NH_2 functional groups are also critical. The decrease in the activity with higher amine loadings can be due to the undesired blocking/poisoning of the surface and/or reduction of NP size [3]. As the particle size decreases, more point defects may exist on the active NP surface rendering it more susceptible towards CO poisoning [12]. CO stripping voltammetry analyses and spectroscopic measurements demonstrated advanced CO poisoning tolerance with MnOx domains. CO poisoning studies on PdAg/N-SiO_2 and PdAg-MnO_x/N-SiO_2 *via*

in-situ FTIR showed less carbonate formation (evident by the smaller 1579, 1352 cm^{-1} IR features upon CO(g) adsorption) on PdAg-MnO_x/N-SiO_2. This suggests that MnO_x is the favored site where CO is attached and these sites act as sacrificial sites that prevent the poisoning of PdAg active metal sites [12].

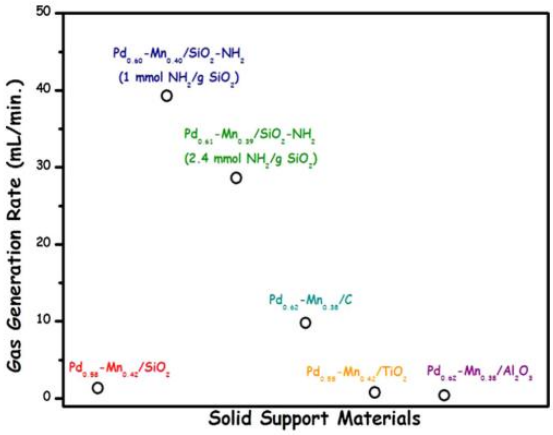

Figure 3. Gas generation rate of catalysts in FA dehydrogenation reaction using catalysts with different support material; $Pd_{0.58}$-$Mn_{0.42}$/SiO_2, $Pd_{0.60}$-$Mn_{0.40}$/SiO_2-NH_2 (1.0 mmol NH_2/g SiO_2), $Pd_{0.61}$-$Mn_{0.39}$/SiO_2-NH_2 (2.4 mmol NH_2/g SiO_2), $Pd_{0.57}$-$Mn_{0.43}$/Al_2O_3, $Pd_{0.58}$-$Mn_{0.42}$/TiO_2 and $Pd_{0.62}$-$Mn_{0.38}$/C [3] (Copyright © Elsevier, 2015**).**

Designing a new multimetallic alloys that can reduce the price of the catalyst is desirable using the synergistic effect that can arise from the combination of a transition metal combined with a noble metal [58]. However, acidic FA solution abrade the first row transition metals and limits their utility. Wang *et. al*. achieved TOF of 80 h^{-1} with 100% H_2 selectivity over CoAuPd/C catalyst bearing 91% conversion without additives and surfactants. Electron transfer from Co to Pd and Au atoms was argued to shift the Fermi level in this system as verified by XPS [59]. A very high conversion (>99%) and activity (730 mol H_2 mol $catalyst^{-1}$ h^{-1}) was also obtained by Zahmakıran *et al*. with CrAuPd/N-SiO_2 catalyst [60].

1.5. Critical Features in Dehydrogenation of FA

1.5.1. Adsorption Characteristics of Metal Surfaces

Intermolecular forces existing on a surface creates a surface energy which can be explained by the Gibbs free energy ($dG \equiv -SdT + VdP + \gamma dA$, $\gamma=(\partial G/\partial A)_{T, P}$). The work that needs to be spent to increase the surface extent is also defined as the surface free energy (γ). The relation between the surface free energy as a function of the geometric distribution of atoms corresponds to the so called Wulff construction. In such crystals surface free energy is expressed as proportional to the length of vector normal to the crystal facet [4]. Principally, Wulff plot is constructed by reuniting points representing the particular surface energy of a plane in that orientation. Since the equilibrium structure will be determined by minimum surface free energy, it is possible to reach the equilibrium shape by tangent lines perpendicular to the circular Wulff plot lines.

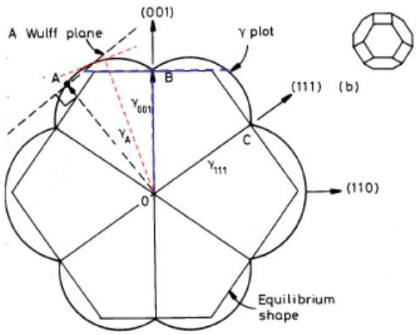

Figure 4. A way to construct Wulff plot [4] (Copyright © Ganghoffer, 2011).

The main driving force for the adsorption is to obtain the minimum surface free energy by attaching adsorbate molecules such as CO and formate anions onto the surface. There are several different geometries that a metal-adsorbate pair can acquire depending on factors such as available sites, electronic structure and coverage.

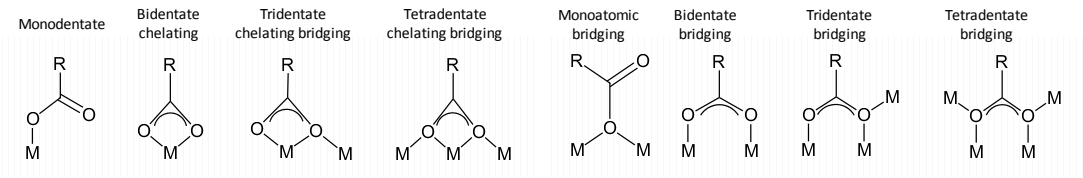

Figure 5. Possible ways of adsorption onto a metal surface with various geometries [5].

The dependence of the catalytic activity and performance on the surface structure is not straightforward; electronic properties as well as structural features of the active metal NPs affect the rate determining step of the reaction. Formates can reveal 2-fold adsorption on flat terrace sites such as Pd (111) facets on the Wullf crystal and lead to the dehydrogenation reaction (Figure 6-a). On the other hand, atop adsorption which is more accessible on coordinatively unsaturated edges and defect sites can create stronger bonds and promote dehydration pathway (Figure 6-b) [6].

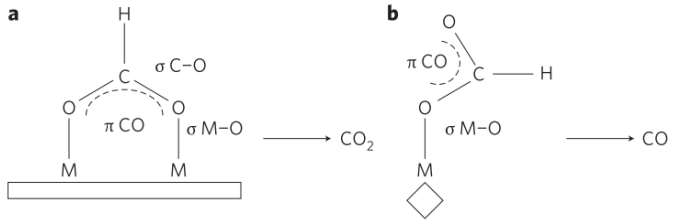

Figure 6. Relation of surface structure with the catalytic decomposition of FA. (a) Bidentate bridging adsorption on flat metal (M) surface. (b) Monodentate adsorption on a surface with coordinatively unsaturated metal (M) sites [6] (Copyright © Nature Publishing Group, 2011).

1.5.2. CO Poisoning at Active Sites

CO generated in the intermediate steps of the FA dehydrogenation reaction is the main reason for the catalyst deactivation. It poisons the catalyst and blocks the active metal sites by strongly binding to those surface active metals. Among the metals

reviewed by virtue of finding a distinguished catalyst, monometallic Pd has the highest catalytic activity [48]. DFT calculations revealed that adsorption energy of adsorbates such as FA or CO increases with the increasing energy of the d-band center of the metal with respect to the Fermi level [61]. Some of the transition metals are evaluated for their catalytic activity in FA dehydrogenation reaction while as a function of the position of their d-band center. The correlation between them established the order in the FA dehydrogenation activity as follows: Ag< Au< Ru≈ Pt< Rh< Pd [6]. Thus, using multi-metallic systems containing Pd, reactant and product adsorption characteristics can be adjusted by tuning the adsorption energy of the metal surface along with the increased distance between neighboring Pd particles. In the systems containing Pd and Ag, Ag atoms can be located between Pd-Pd-Pd (*i.e.* all-Pd) 3-fold sites of the Pd (111) facets, thus preventing the strong adsorption of adsorbates on all-Pd 3fold sites. 3-fold adsorption is especially undesired due to the greater adsorption strength of CO on such sites that can lead to catalytic poisoning of the active metal particles with CO.

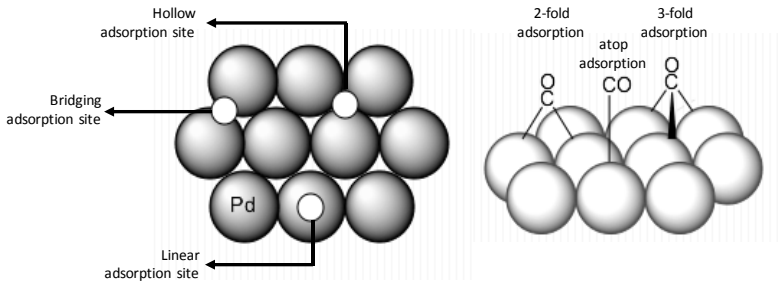

Figure 7. A simple representation of adsorption geometries of CO onto Pd nanoparticles.

CO can adsorb on a surface with different geometries (Figure 7) that can be monitored using FTIR. The vibrational frequency of the CO molecule changes simultaneously with coordination number of the metal. With the increasing electron

density of the d-orbitals of Pd, electron back-donation from Pd to CO antibonding orbital π^* increases and consequently bond order of CO lowers (Figure 8). The vibrational frequency of a classical oscillator is expressed as follows;

$$V = \frac{1}{2\pi}\left(\frac{k}{\mu}\right)^{1/2}$$

μ being the reduced mass and k is force constant where the latter is directly proportional to bond order of the oscillator. Decrease in bond order implies the weakening of the bond, lessening the force constant along with the vibrational frequency of CO. Typical vibrational frequencies of atop, 2-fold and 3-fold adsorbed CO are in the range of 2100-1900 cm^{-1}, 1900-1800 cm^{-1}, 1800-1700 cm^{-1} respectively [7].

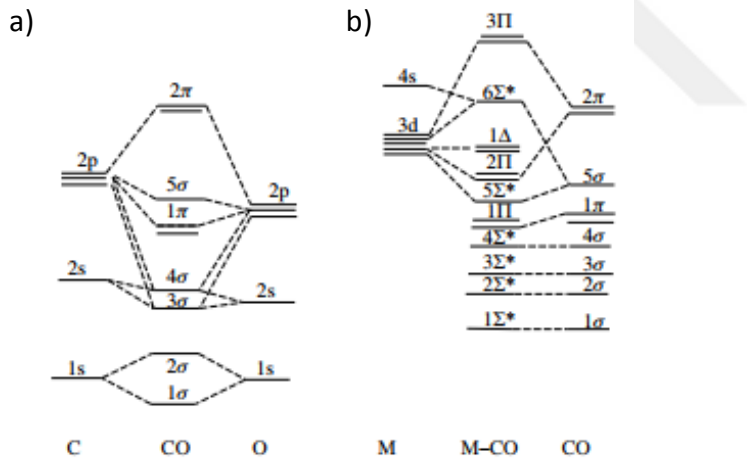

Figure 8. Molecular orbitals of (a) gas phase (free) CO and (b) linear M-CO adsorption system [7] (Copyright © John Wiley and Sons, 2003).

1.5.3. Nature of FA and Formates

HCOOH and its isotopically labelled counterparts are non-symmetrical planar molecules having C_s symmetry. 5 atoms in each of these molecules give rise to 15 degrees of freedom being 3 translational, 3 rotational and 9 vibrational modes

(Figure 9). 4 bonds result in 4 stretching vibrations while the rest corresponds to bending modes. On the other hand, formates which are more symmetrical and have 12 degrees of freedom with 6 vibrational modes.

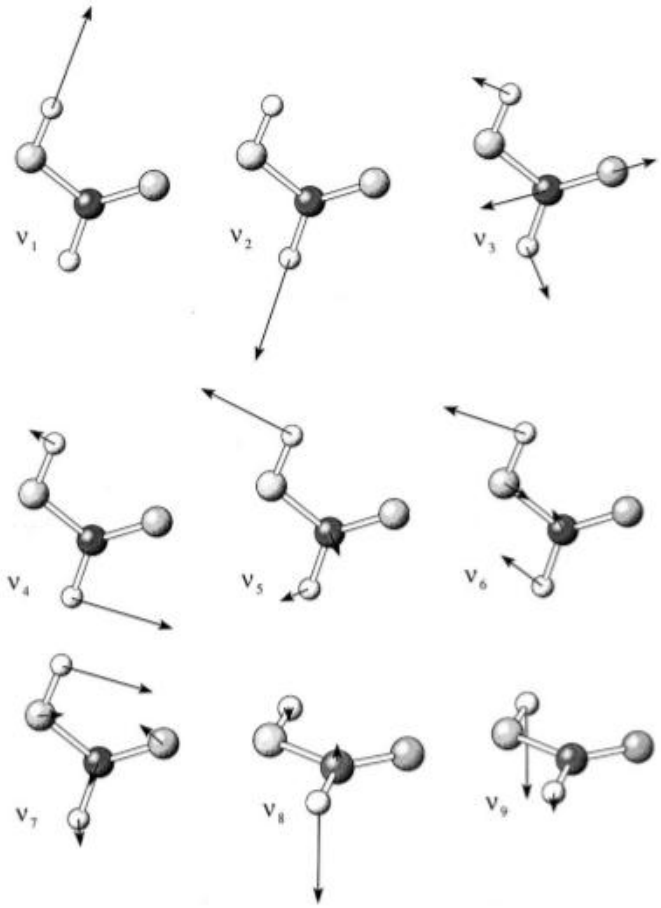

Figure 9. Normal modes of vibration of FA using aug-cc-pVTZ basis set in MP2 level calculation [8] (Copyright © Elsevier, 2002).

Molecular formic acid can possess different structures like monomers, dimers as well as polymers depending on the surface coverage and can be monitored by the O-H vibrations. O-H vibrations are related to the hydrogen bonding between monomers and can reveal the form of molecular FA. Frequency of π(OH) which is out of phase vibration of FA, changes with oligomerization/polymerization. π(OH) increases from 636 cm^{-1} for FA monomer to 917 cm^{-1} for FA dimer, 974 cm^{-1} for β-

polymeric FA and 974 cm^{-1} for α-polymeric FA (Figure 10) [9]. The structure of FA on Pt (111) is dependent on FA coverage, it alters from α-polymeric to monomeric gradually with decreasing coverage. On the other hand, on Ag (111), FA stays monomeric with increasing surface coverage while it forms β-polymer on clean Ag film. This may be due to the weaker interaction of FA with the Ag surface [9].

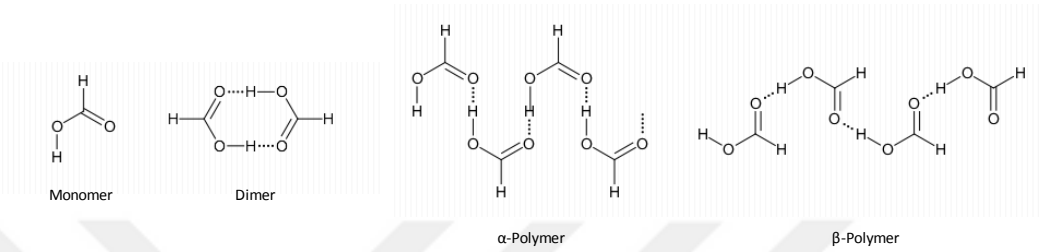

Figure 10. The structures that can be attained by molecular FA [9].

Formates appear when the acidic proton in FA is removed. They can adsorb on to a metal surface mostly in monodentate, bidentate chelating and bidentate bridging forms. Bidentate chelating occurs when more than one atom of FA is bonded to the same metal atom, while bridging results from the donation of electron pairs from FA to more than one Lewis acids at the same time.

C_{2v} symmetry of the free formate ion is lowered with the adsorption onto a surface. Upright C-H bond in α-formate which has the symmetrical bidentate configuration maintains its C_{2v} symmetry. Tilting the molecule around the molecular plane lowers the symmetry due to the disappearance of a mirror plane and creates C_s (1) in β-formate. If the mirror plane is kept vertical to the metal surface, γ-formate having C_s (2) symmetry is obtained. When there is no other symmetry element, adsorbed structure assumes C1 symmetry which is seen in δ-formate [9]. Reducible and irreducible representations of these different point groups were determined and the vibrational modes were found using relevant character tables. The normal modes of vibrations were assigned for each representation and IR active modes are obtained.

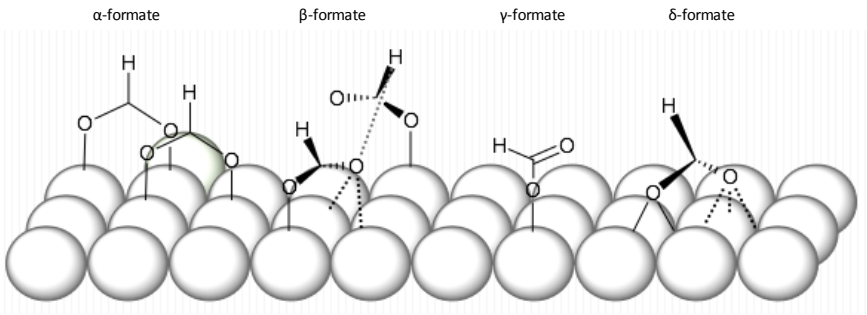

Figure 11. Types of adsorbed formates on Ag (111) surface [9].

The character of adsorbed formate can also be monitored from C-O bond since the vibrational frequency of this bond will change with the bond order. The vibrational frequency difference between asymmetric and symmetric vibrations of OCO (ν_{as}(OCO)- ν_s (OCO)) is related to the similarity between 2 C-O bonds in the molecule. The larger the separation, the weaker the interaction of free oxygen with the surface ($\Delta(\nu_{as}(OCO)- \nu_s(OCO))$ ~200 cm^{-1} (δ-formate), ~240 cm^{-1} (β-formate), ~320 cm^{-1}(γ-formate)) [9]. These different adsorbed formate species were found to be coverage-dependent and can transform to one another. α-formate observed at low coverages is converted to β-formate at moderate coverages. When the surface is saturated with β-formate, δ-formate starts to be formed. Adsorbed formates on a metal center in bidentate bridging configuration have C_{2v} symmetry point group and six normal modes of vibrations (Figure 12).

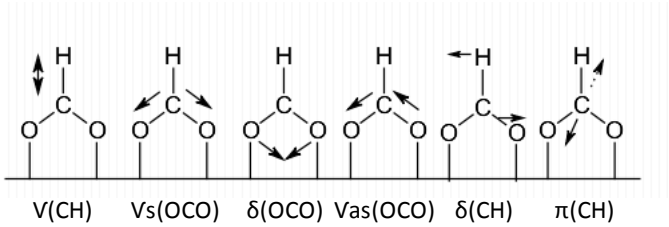

Figure 12. Adsorption of formate onto a surface in bidentate bridging geometry and related vibrational modes [10].

CHAPTER 2

EXPERIMENTAL

2.1. Catalyst Synthesis Procedure

All the catalysts were synthesized by Zahmakıran Research group at Yüzüncü Yıl University using wetness impregnation method followed by reduction steps. Active metal (M) loading was kept at 2%(w/w) for monometallic active sites (M/APTS/MnOx/SiO_2) while the total active metal loading was also 2% (w/w) for bimetallic (M1M2/APTS/MnOx/SiO_2) and trimetallic active sites (M1M2M3/APTS/MnOx/SiO_2).

Type of Catalyst	**Name of Catalyst**
APTS/MnO_x/SiO_2	APTS/MnO_x/SiO_2
M/APTS/MnO_x/SiO_2	Pd/APTS/MnO_x/SiO_2
	Ag/APTS/MnO_x/SiO_2
	Cr/APTS/MnO_x/SiO_2
M1M2/APTS/MnO_x/SiO_2	PdAg/APTS/MnO_x/SiO_2
M1M2M3/APTS/MnO_x/SiO_2	PdAgCr/APTS/MnO_x/SiO_2

Table 2. Compositions and acronyms of the synthesized catalysts.

2.1.1. Synthesis of APTS/MnO_x/SiO_2 Support Material without Active Sites

250 mL SiO_2 (Silicon Dioxide, Merck, 230-400 mesh) and 40.0 mL deionized water (Milli-Q Water Purification System) were transferred into a beaker and 1.14 mmol $MnCl_2 \cdot 2H_2O$ (manganese (II) dichloride dihydrate, Sigma-Aldrich) corresponding to 20% (w/w) mass percent of SiO_2 was added to the mixture while stirring for 2 h at a constant rate (600 rpm) at room temperature. The reduction was performed by adding 19 mmol $NaBH_4$ (716 mg) (Sodium Borohydride, Sigma-Aldrich) dissolved in 5.0 mL deionized water into the initial solution. After the completion of the reduction, solid part was separated by vacuum filtration using Whatmann-5 filter paper, washed with 50.0 mL deionized water and dried under 80 ^oC, 10^{-1} Torr in vacuum drying oven for 3 h. Dried solid was taken into a volumetric flask that containing 50.0 ml ethanol (C_2H_5OH) for surface functionalization. 0.65 ml APTS, $(H_2N(CH_2)_3Si(OC_2H_5)_3$ (3-aminopropyltriethoxysilane, Sigma-Aldrich) was added and mixture was kept under 80 ^oC for 24 h in the condenser. At the end of 24 hours, solid was separated with vacuum filter using Whatmann-5 filter paper, washed with 50.0 mL deionized water and dried under 80 ^oC, 10^{-1} Torr in vacuum drying oven for 3 h. In order to minimize oxide formation on the metal surface before the catalytic reaction, material was stored under dry nitrogen box (O_2<5ppm, H_2O<10ppm) until the activity measurement.

2.1.2. Synthesis of M/APTS/MnOx/SiO_2 Monometalllic Catalysts

The same procedure prior to the storage under dry nitrogen box is applied and repeated as described above for the synthesis of the monometallic catalysts. 2% (w/w) weight percent metal (M) loading is carried out for M/APTS/MnOx/SiO_2 (M=Pd, Ag, Cr). After the APTS introduction, filtration, washing and drying the sample, solid was

transferred into 10.0 ml deionized water containing 2% (w/w) metal (M) corresponding to M=17.2 μmol $Pd(NO_3)_2 \cdot H_2O$ (4.43 mg) (Palladium (II) Nitrate Hydrate, Sigma-Aldrich), M=5.7 μmol $Cr(NO_3)_3 \cdot 9H_2O$, (2.29 mg) (Chromium (III) Nitrate Nonahydrate, Sigma-Aldrich), M=5.8 μmol $AgNO_3$ (0.98 mg) (silver(I) nitrate, Sigma-Aldrich). The solution was stirred under constant rate (600 rpm) for 2 h at room temperature. The reduction was initiated by the addition of 19 mmol $NaBH_4$ (716 mg) dissolved in 5.0 ml deionized water. Solid was separated by vacuum filtration using Whatmann-5 filter paper, washed with 50.0 mL deionized water and dried under 80 ^oC, 10^{-1} Torr in vacuum drying oven for 3 h after the reduction was completed. In order to minimize oxide formation on the metal surface before the catalytic reaction, material was stored under dry nitrogen box (O_2<5ppm, H_2O<10ppm) until the experiment.

2.1.3. Synthesis of M1M2/APTS/MnOx/SiO_2 Bimetalllic and M1M2M3/APTS/MnOx/SiO_2 Trimetalic Catalysts

The same sample preparation method was used as it described above except the variation of the type and the number of the active metal salts. Total active metal (M) loading was kept 2% (w/w) while M1 being Pd, M2 is Ag and M3 is Cr.

2.2. Analytical Techniques & Instrumentation

2.2.1. Catalytic Performance Measurements

The catalytic activities of the synthesized materials were acquired by Zahmakıran research group using a reactor system by following the gas produced over time. The reactor system was resistant to high pressures allowing remote control of temperature, pressure and stirring rate *via* computer. FA dehydrogenation was

achieved at a particular temperature and stirring rate in a closed reactor and the volume of gas produced was monitored with high sensitivity (~0.001 psi) within a specific time interval. The data was collected using ORDEL software via RS-232 connection to the computer. Prior to the reaction, 100 mg catalyst was transferred to the reaction flask. Water was added and the mixture was stirred to reach thermal equilibrium. After 15 min, FA aqueous solution was added to the autoclave with a gas-tight syringe. The reaction started immediately with 10.0 ml 0.2M FA aqueous solution and 100 mg catalyst by constant stirring at 600 rpm.

Gas Chromatography (GC) was performed with FID-2014 and TCD-2014GC analyzers (Shimadzu) for the selectivity of the high activity catalyst in FA dehydrogenation reaction. Decomposition products of FA in gas phase were fed through GC and the produced gas was determined with the analysis. In order to confirm the results, as a second control mechanism, the gas also was circulated to FTIR spectrometer (Shimadzu IR-Affinity).

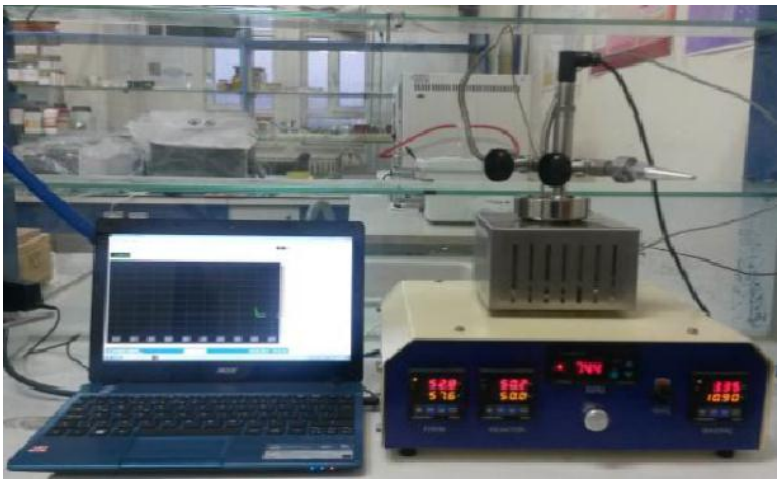

Figure 13. High pressure reactor with heat control and stirring adjustments used in the catalytic performance experiments for dehydrogenation of FA.

2.2.2. Structural Characterization Techniques

An extensive set of structural and functional characterization techniques were employed to analyze the synthesized materials including advanced surface sensitive and *in-situ* analytical techniques that will be described further in the following sections.

2.2.2.1. X-Ray Diffraction (XRD) Analysis

XRD Patterns of the powder catalyst samples were acquired via Rigaku diffractometer, combined with a Miniflex goniometer, having X-ray source providing Cu Kα radiation (λ=1.5418Å, 30 kV, and 15 mA) which was aligned and aimed to the pressed powder sample on a quartz slide. The sample scans were executed in 10-80° 2θ range with a scan rate of 0.01 deg. s^{-1}. Diffraction patterns were analyzed with a separate software searching Joint Committee on Powder Diffraction Standards (JCPDS) cards provided by International Centre for Diffraction Database (ICDD).

2.2.2.2. Brunauer Emmett Teller (BET) Specific Surface Area Analysis

Micromeritics ASAP 2000 gas sorption and porosimetry system was employed for the specific surface area (SSA, m^2/g) measurements using the five-point Brunauer-Emmett-Teller (BET) method. In order to remove physisorbed species on the powder catalyst, samples were initially pretreated under vacuum first at RT for 1 h then at 70°C for 5 hours to eliminate water.

2.2.2.3. Raman Spectroscopy

PdAgCr-MnO_x/SiO_2-NH_2 catalyst was analyzed with HORIBA Jobin Yvon LabRam HR 800 confocal raman spectrometer with 532.1 nm green Nd:YAG laser

tuned to 20 mW laser power. The device consists of BX41 microscope, 800 mm focal length spectrograph and a CCD detector. Powder catalyst was distributed onto a glass microscope slide in a compact manner. ×10 objective was used to focus the light onto the powder sample. Continuous calibration of the spectrometer was achieved by fine-tuning the zero order position of the grading. All Raman spectra were acquired within 200 - 1700 cm^{-1} with an acquisition time of 213 s and a spectral resolution of 2 cm^{-1}. The rest of the catalysts were examined using WITec alpha 300R confocal Raman spectrometer with 1064 nm He-Ne laser.

2.2.2.4. TEM-EDX Measurements

The size, morphology, and the composition of the best performing catalyst were studied with different microscopic methods. Surface morphology of the PdAgCr/APTS/MnOx/SiO2 catalyst was investigated *via* low resolution TEM images taken at 120 kV with JEOL JEM-200CX transmission electron microscope. The mean particles size of PdAgCr NPs on the catalytic material surface was detected with the analysis of >100 non-touching particles via NIH image program. The sample was imaged further using high resolution JEOL JEM-2010F transmission electron microscope working at 200 kV. Elemental composition of the nanostructures was determined with HAADF-STEM (High Angle Annular Dark Field- Scanning Transmission Electron Microscopy) and STEM-EDX (Scanning Transmission Electron Microscopy-Energy Dispersive X-Ray) operating likewise. STEM-EDX data were collected with Oxford EDX system and treated via a software (Inca). The samples for those analyses were prepared on a copper-coated carbon TEM grid by the evaporation of solvent remaining on the dilute catalyst suspension.

2.2.2.5. XPS Measurements

Near Ambient Pressure-XPS (NAP-XPS) data of the PdAg and PdAgCr samples were recorded with a SPECS EnviroESCA spectrometer using a hemispherical electron analyzer (E_{pass}=100 eV) and Al Kα x-ray irradiation (hν= 1486.61 eV). During the measurement of all samples and regions, the background pressure was 1.9 mbar with air flow of 1 ml/min.

2.2.2.6. ICP-EOS Analysis

Metal loadings (Pd, Ag, Cr, Mn) on the surface of the solid support were detected by Zahmakıran research group using ICP-OES (Inductively Coupled Plasma-Optical Emission Spectrometry) analytical technique by Leeman Labs, Direct Reading Echelle. Prior to the measurements, the catalysts were dissolved entirely under mild heating in HNO_3/HCl (1/3 v/v) mixture.

2.2.3. Functional Characterization

The interaction of the catalyst surfaces with reactants and products were monitored via in-situ FTIR for functional characterization.

2.2.3.1. Spectroscopic Reactor Set-up

FTIR spectroscopic measurements were performed in a custom designed catalytic system based on FTIR spectrometer (Bruker Tensor 27) using Silicon carbide source, operating with a high sensitivity Hg-Cd-Te (MCT) mid-IR (MIR) detector functioning via liquid nitrogen (LN2), coupled with batch-type in-situ reactor and a quadruple mass spectrometer (QMS, Stanford Research Systems, RGA 200). The spectrometer with gold-plated mirrors consist of optical windows and beam splitter

made from KBr while the windows of the reactor cell is BaF_2.

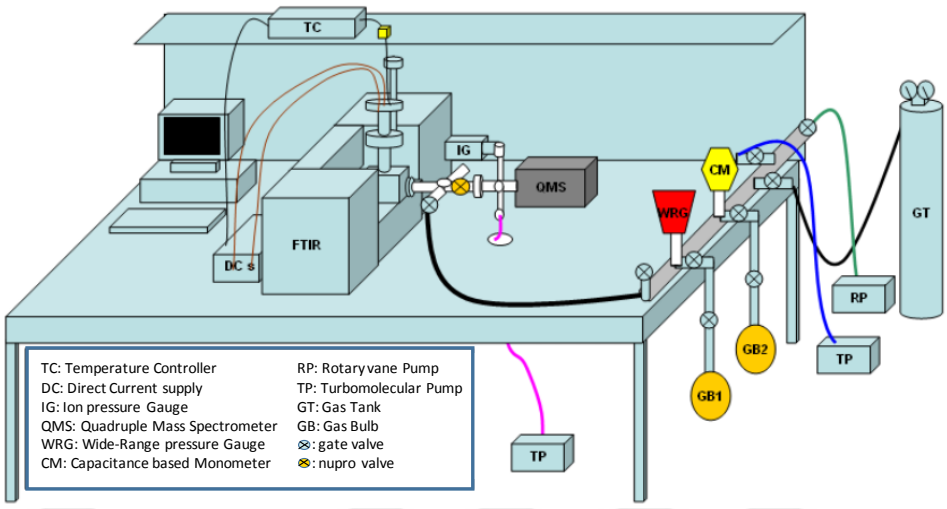

Figure 14. Illustrative design of in-situ FTIR and TPD analysis system [11].

Pressures at different regimes are measured through four separate gauges namely, cold cathode gauge (10^{-9}-10^{-3} Torr), pirany gauge (10^{-3}-1000 Torr), Baratron type capacitance gauge (1-1000 Torr) and Bayerd Albert type ionization gauge (10^{-2}-10^{-10} Torr), the latter being mainly used with mass spectrometer. Two turbo-molecular and three rotary-vane pumps established the vacuum components of the system. Manifold and reactor chamber were pumped first with a rotary-vane pump to get rid of the high pressure followed by additional pumping *via* turbo-molecular pump. The second turbo-molecular pump was run for the QMS when it was needed while other two rotary-vane pumps were constantly operated prior to the turbo-molecular pumps as the fore pumping stage.

A high purity photo-lithographically etched tungsten grid (TechEtch, USA, P/N PW10379- 003) was used to hold the powder catalysts in position. Thermocouple wires (K-type alumel-chromel, Omega Engineering, Inc.) were welded onto tantalum foil attached on the top of W-grid. W-grid configuration was secured to copper sample holder legs to connect/conjoin the electrical vacuum feedthrough. An adjustable DC power supply and a computer-controlled PID (Gefran 600-DRRR) were employed to

heat the sample attached on the W-grid to the desired value linearly. An external heating system was employed so as to remove adsorbed chemicals as well as water from the surface of the reaction chamber and manifold walls.

2.2.3.2. *In-situ* FTIR Adsorption Experiments

Gases (CO(g)) and liquids (FA, DCOOH, HCOOD, DCOOD) to be investigated were transferred to special glass containers equipped with from metal to pyrex adaptors and mounted to the system through VCR face seal fittings (Swagelok) using copper or stainless steel gaskets. The isotopically labelled, deuterated FA samples were transferred to these glass bulbs in a glove box after all the equipment was held under vacuum for 24 h in order to avoid contamination of the glove box by the atmospheric species.

In-situ FTIR measurements were acquired in transmission mode at 303 K (*i.e.* 30 $^{\circ}$C) and spectra were collected with 128 scans, (4 cm^{-1} resolution and 3 mm aperture size). Catalysts were placed into the *in-situ* FTIR reactor set-up and outgassed to very low pressures (~10^{-7} Torr). However, prior to the experiments with isotopically labelled species, inner walls of the gas lines were slightly heated to 40 $^{\circ}$C with heating tapes in order to minimize condensation of the gas on the inner walls of the system.

2.2.3.3. Gas Phase *in-situ* FTIR Experiments

5 Torr of gas was introduced directly to the system *via* special valves after pumping out all of the atmospheric species in the reactor. Gas phase HCOOH (Merck > 96%), DCOOH (Cambridge Isotope Laboratories, CIL Inc, 98%, <5% H_2O), HCOOD (CIL, Inc, 98%, <5% D_2O), DCOOD (CIL, Inc, 98%, <5% D_2O), were investigated separately *via in-situ* FTIR at 303 K.

2.2.3.3.1. *In-situ* FTIR Experiments: FA Adsorption

5 Torr of FA vapor or its isotopically labelled counterparts were introduced over a fresh PdAgCr/MnO_x-SiO_2 NH_2 catalyst sample (10-20 mg) by first dosing to the manifold and then to the reactor chamber. All the FTIR spectra were obtained at 303 K.

2.2.3.3.2. *In-situ* FTIR Experiments: CO Adsorption

20 Torr of CO (Air Products, >99.995%) was dosed onto a fresh catalyst sample at 303 K and in-gas spectra were taken in repeated measurement mode for 65 min. After the gas phase CO was pumped out, 5 Torr of FA vapor was introduced over the CO poisoned catalyst for 30 min. The adsorption of FA on poisoned catalyst was investigated by degassing gas phase FA.

CHAPTER 3

RESULTS AND DISCUSSION

3.1. Activity Measurements

Dehydrogenation reaction with 10 ml, 0.2 M FA aqueous solution and 100 mg catalyst were examined by volumetrically monitoring the produced gas over time with metal-free, monometallic, bimetallic, and trimetallic catalysts.

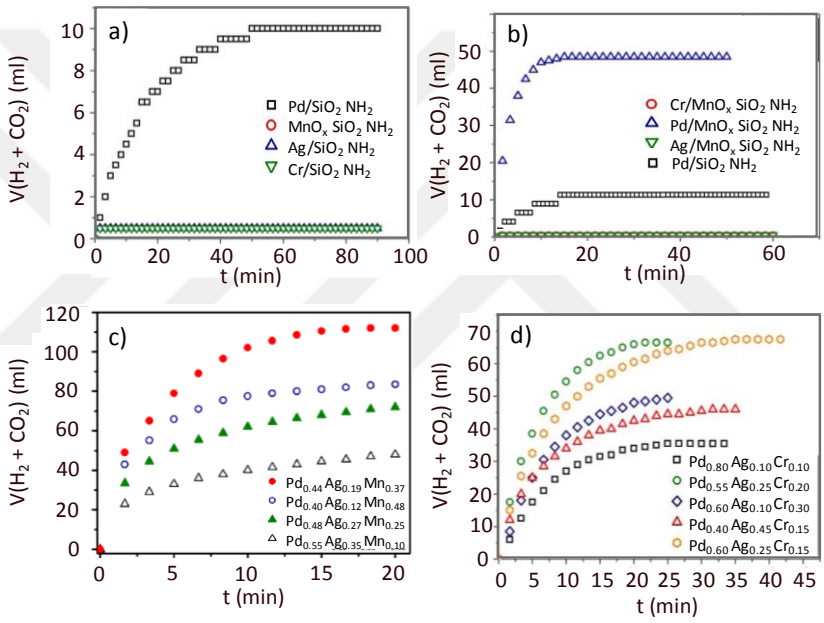

Figure 15. Graph of gas produced over time in dehydrogenation of 10.0 ml 0.2 M FA solution with 100 mg (a) metal-free MnO_x-SiO_2-NH_2, monometallic Pd/SiO_2-NH_2, Ag/SiO_2-NH_2 and Cr/SiO_2-NH_2 without promoter, (b) monometallic Pd-MnO_x/SiO_2-NH_2, Ag-MnO_x/SiO_2-NH_2, Cr-MnO_x/SiO_2-NH_2 catalysts with promoter in comparison with monometallic promoter-free Pd/SiO_2-NH_2, (c) bimetallic PdAg-MnO_x/N-SiO_2 catalysts as a function of metal loadings [12] (Copyright © American Chemical Society, 2015), (d) trimetallic PdAgCr-MnO_x-SiO_2-NH_2 catalysts with different metal compositions.

Metal-free MnO_x-SiO_2-NH_2 and monometallic promoter-free Pd/SiO_2-NH_2, Ag/SiO_2-NH_2, Cr/SiO_2-NH_2 samples were compared in terms of their catalytic activities in Figure 15a. While MnO_x, Ag and Cr have no activity in the absence of other compositional components, Pd/SiO_2-NH_2 produced limited amount of gas, suggesting that Pd is the active site. Pd, Ag and Cr atoms are coupled with MnO_x promoter to obtain monometallic catalysts (Figure 15b). Pd was the only catalyst in this group consistent with the fact that Pd is the active site. Moreover, the activity of Pd bearing monometallic catalyst was improved almost 5 times after MnO_x incorporation compared to the analogous material without MnO_x. Ag metal was incorporated into the model catalyst system in order to suppress CO poisoning of active Pd metal sites. Optimization of the Ag loading in the PdAg bimetallic catalysts also enhanced the activity further (Figure 15c). Enhancement of the catalytic properties was further strengthened by the addition of a third active metal site (i.e. Cr). Rather than using precious metals such as Au, Pt, Ir, Rh, Ru *etc.* Cr was used as a cost-effective additive. Synthesized trimetallic catalysts with varying metal loadings were tested for FA dehydrogenation (Figure 15d). $Pd_{0.55}Ag_{0.25}Cr_{0.20}$-$MnO_x$/$SiO_2$-$NH_2$ catalyst showed the best catalytic performance. The gas generated was fed to GC to confirm CO_2 formation. The optimized catalytic system was found to dehydrogenate FA with 100% selectivity at RT.

3.2. Structural Characterization

3.2.1. XRD Analysis

XRD patterns of synthesized materials were given in Figure 16 with Savitzkey-Golay smoothing. Disordered nature of the silica support material and its active metal functionalized derivatives (Pd, PdAg, PdAgCr) was clearly visible. MnO_x/SiO_2-NH_2

support material has diffraction peaks associated with amorphous SiO_2 (JCPDS # 07-089-3606), tetragonal MnO_2 (JCPDS # 00-044-0141) and Mn_2O_3 (JCPDS # 00-041-1442). Diffraction peak at $2\Theta=40^o$ (JCPDS # 04-016-4693) which is a characteristic signal for Pd (111) facets is observed, while the characteristic diffraction signal for Ag (111) at $2\Theta=38^o$ was not visible [58], [62]. Upon introduction of Ag to the Pd-MnO_x/SiO_2-NH_2 catalyst, Pd diffraction peak shifted from 38^o and appeared in between 38^o and 40^o suggesting PdAg alloy formation [12], [58], [62].

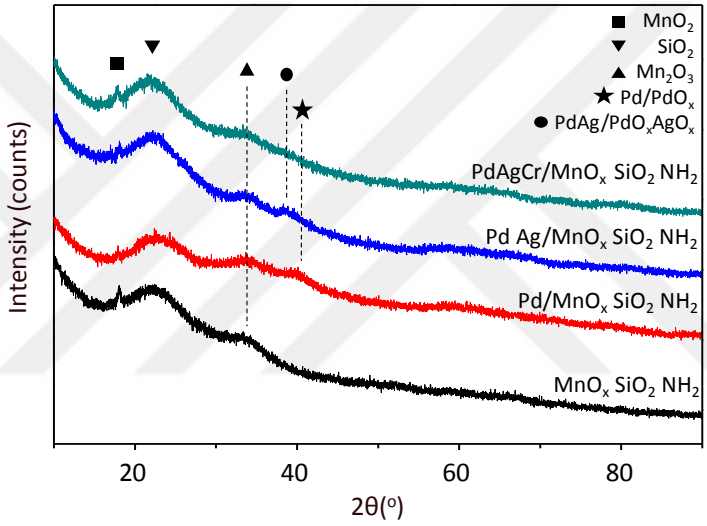

Figure 16. XRD patterns of MnO_x/SiO_2-NH_2 and its active metal NP (Pd, PdAg, PdAgCr) functionalized counterparts.

3.2.2. BET Analysis

The BET specific surface areas of the precious metal catalysts are given in Table 3. Proximity of the surface areas of three catalysts are apparent. Addition of new metals may infuse into the pores of the powder sample and cause a slight decrease in the SSA. Although surface area is not directly related to the activity of the catalyst, high surface area of these materials can promote a better distribution of the active metals that is also in agreement with the current TEM results. Better distribution of

the active sites can facilitate the FA dehydrogenation by providing individual sites for FA adsorption.

Catalyst	BET Specific Surface Area (m^2/g)
Pd-MnO_x/SiO_2-NH_2	267
PdAg-MnO_x/SiO_2-NH_2	249
PdAgCr-MnO_x/SiO_2-NH_2	251

Table 3. BET specific surface areas (m2/g) of the selected catalysts.

3.2.3. Raman Spectroscopic Analysis

Raman spectrum of PdAgCr-MnO_x/SiO_2-NH_2 catalyst is presented in Figure 17. Major peaks in manganese oxide systems lie between 520-650 cm^{-1} with smaller peaks that can vary in a broad range [63]. Broadness of the MnO_x-related signals indicates varying oxidation states for Mn, possibly corresponding to Mn_2O_3 and MnO_2. The peak at 645 cm^{-1} is associated with PdO species showing that Pd active sites were partially oxidized [64], [65]. Signals within 400-500 cm^{-1} can be attributed to the oxidized Ag (*i.e.* Ag_2O and/or $PdAgO_x$) [66], [67]. Cr_2O_3 features are typically observed at 300, 335-340 and 551 cm^{-1} [68] were also present as minor features for the Raman spectrum of the PdAgCr-MnO_x/SiO_2-NH_2 catalyst. Additionally, the sharp peak at 237 cm^{-1} is consistent with the presence of Cr (VI) species [69] whereas 875-740 cm^{-1} can be assigned to Si-O modes of the support [70].

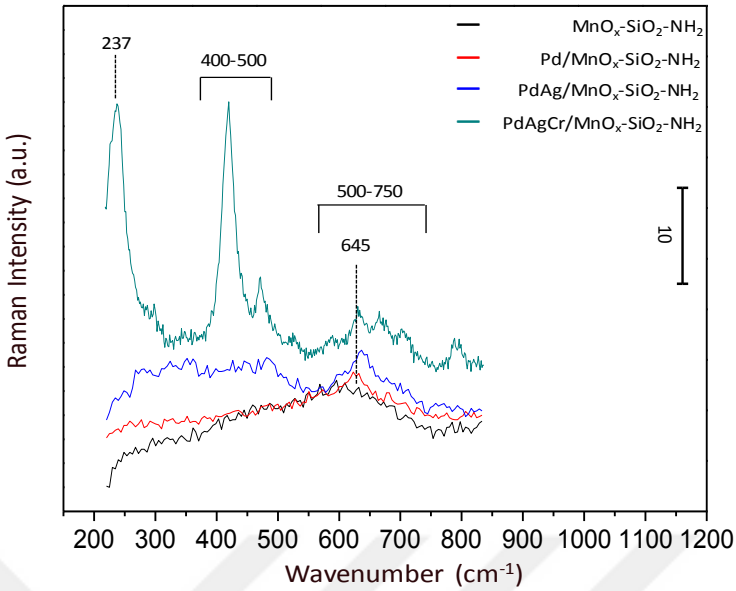

Figure 17. Raman spectra of MnOx/SiO2-NH2 (black), Pd-MnOx/SiO2-NH2 (red), PdAg-MnOx/SiO2-NH2 (blue), PdAgCr-MnOx/SiO2-NH2 (cyan) catalyst with x10 objective, 20 mW laser power.

3.2.4. TEM-EDX Analysis

Exceptionally active PdAgCr-MnO_x/SiO_2-NH_2 catalyst was also analyzed with TEM in order to acquire information about the size of the NPs (Figure 18). PdAgCr and MnO_x nanoparticles existing on the surface were detected. Average particle size of PdAgCr NPs on the surface of the catalyst were determined by the statistical investigation of the images taken (Figure 18-d). Average NP particle size was found to be 3.7 ± 0.9 nm with a fairly narrow particle size distribution indicating good monodispersity.

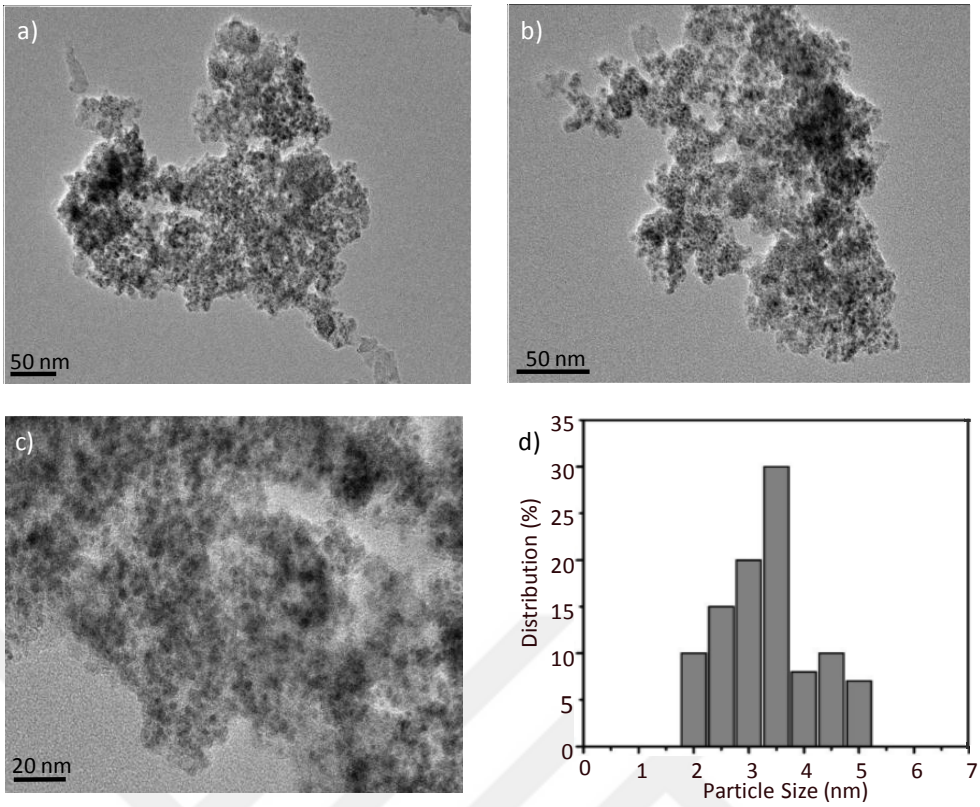

Figure 18. (a-c) Low resolution TEM images of PdAgCr-MnO_x/SiO_2-NH_2 catalyst and (d) PdAgCr particle size distribution.

High-resolution HRTEM images were obtained from the same catalyst to investigate the shape and morphology of the NPs. Crystalline nature of PdAgCr NPs can be noticed from Figure 19-b revealing a typical cuboctehedral structure.

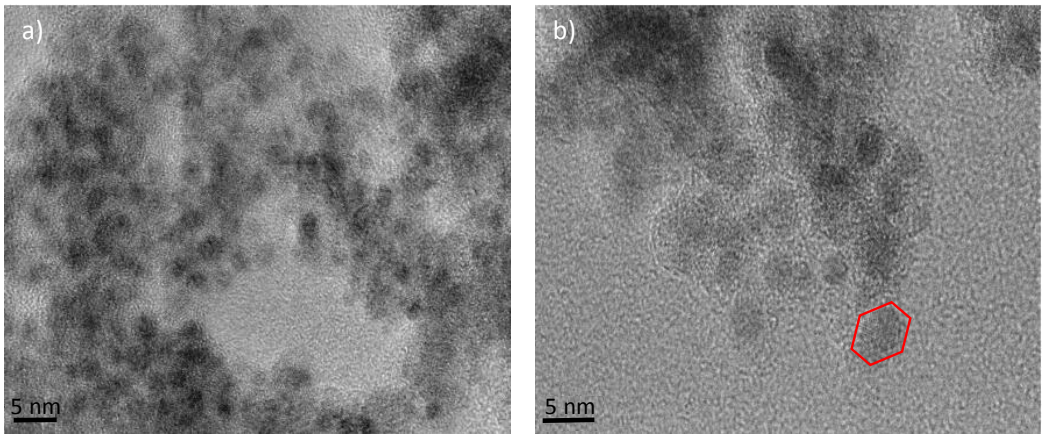

Figure 19. HRTEM images of PdAgCr-MnO_x/SiO_2-NH_2 catalyst.

The elemental composition of the catalytic material is investigated with and STEM-EDX analysis. Figure 20 illustrates the HAADF-STEM images as well as STEM-EDX spectra collected from different points of the PdAgCr-MnO_x/SiO_2-NH_2 sample. EDX data presented in spectrum 1 in Figure 20 suggests the presence of PdAgCr alloy NPs where all of the active metals namely Pd, Ag, and Cr co-exist on the same particle. On the other hand, Spectrum 2 in the same figure is a representative region of the support surface lacking active NPs but containing MnO_x.

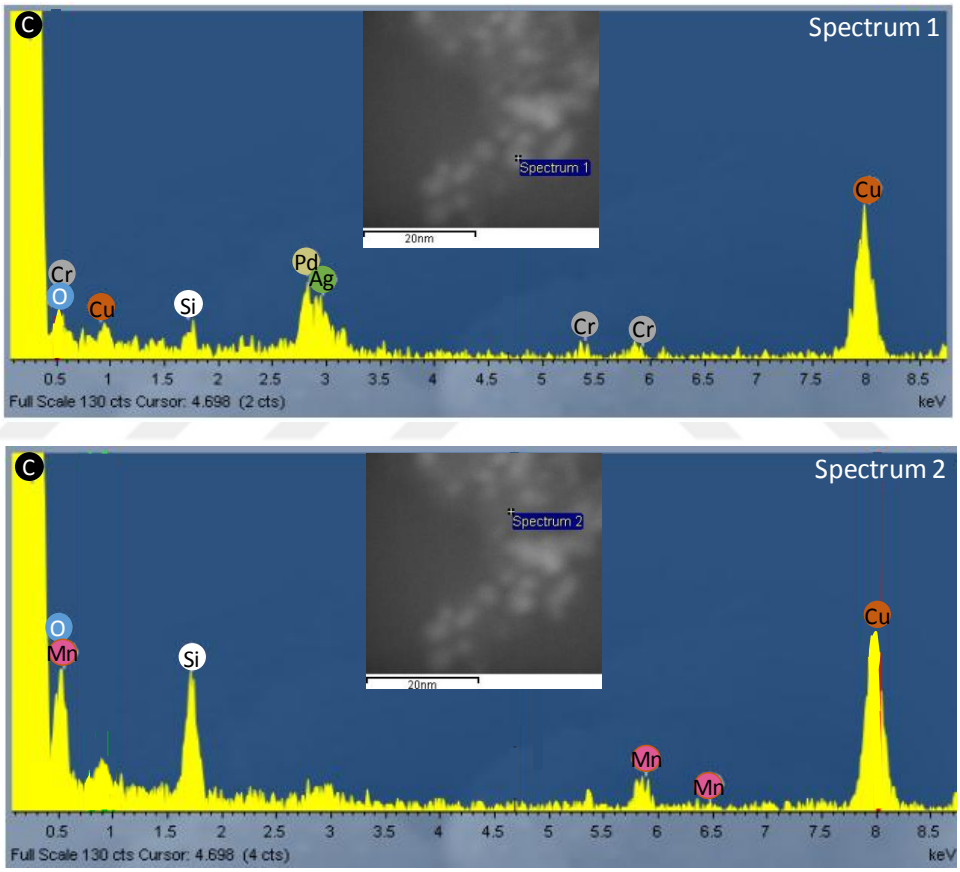

Figure 20. HAADF-STEM images and STEM-EDX spectra collected from specified points of PdAgCr-MnO_x/SiO_2-NH_2 catalyst.

3.2.5. XPS Analysis

PdAg and PdAgCr samples were analyzed by Ambient Pressure-XPS (AP-XPS). C1s signal at 284.6 eV due to the adventitious carbon was taken as the reference

[71] for the calibration of all Binding Energy (B.E.) positions. When we look at manganese signals, $2p_{3/2}$ signal for both samples were observed at 641.5 eV. This signal can be attributed to Mn_2O_3 (Figure 21-a) [72]. However, it must be noted that $2p_{3/2}$ signals for various manganese oxide are very close to each other and the possibility of having multiple oxidic forms of manganese (*e.g.* Mn(II) and Mn(III)) should not be excluded. Signals at 102.2 eV for both samples belong to the Si $2p_{3/2}$ signal and they seem to be shifted by 3.3 eV to the higher B.E. from the Si^0 state (Figure 21-b) [73]. It should be noted that the corresponding chemical shift of the Si $2p_{3/2}$ signal for SiO_2 is *ca.* 4.2 eV [71]. This observation suggests that the main Si $2p_{3/2}$ signal in the spectrum is not due to SiO_2 (*i.e.* Si^{4+}), but rather due to a different Si species with a slightly lower oxidation state (*i.e.* Si $^{(4-x)+}$). This observation can be readily explained by considering the 3-(aminopropyl) triethoxysilane ($H_2N(CH_2)_3Si(OC_2H_5)_3$, APTS) groups which were used to functionalize the catalyst surfaces with basic -NH_x species during the synthetic protocol. It is apparent that the Si species in the APTS structure are not fully oxidized due to the $H_2N(CH_2)_2CH_2$-ligand coordinating to the central Si atom with a relatively poor electron withdrawing power. Presence of this latter ligand in the APTS structure leads to silicon oxidation state which is slightly reduced with respect to Si^{4+}. This observation also points out the fact that APTS functional groups effectively coat the catalyst surface.

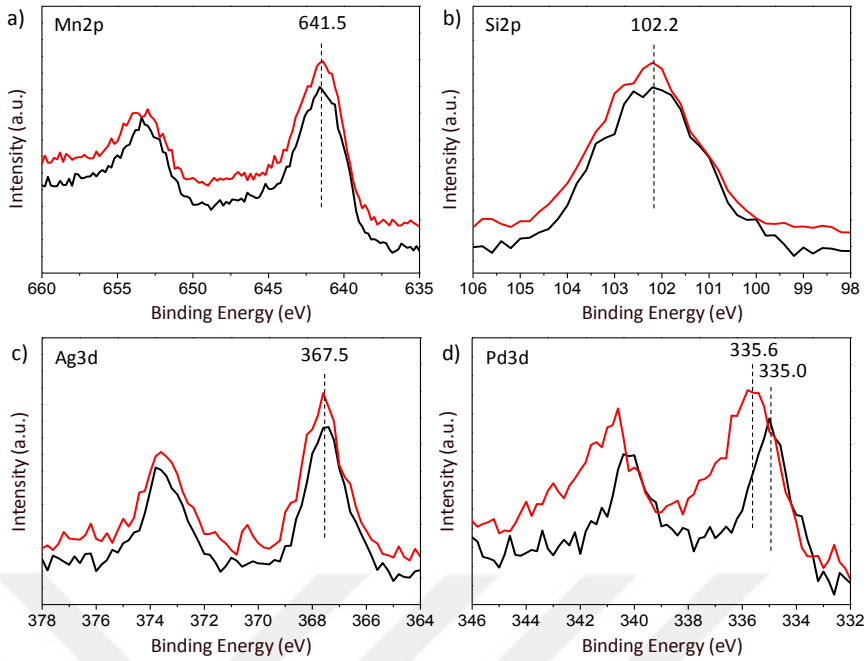

Figure 21. AP-XP spectra of PdAg-MnO_x/SiO_2-NH_2 (black) and PdAgCr-MnO_x/SiO_2-NH_2 (red) catalysts in (a) Mn2p, (b) Si2p, (c) Ag3d, and (d) Pd3d regions.

$Ag3d_{5/2}$ signal for both PdAg and PdAgCr samples was observed at 367.5 eV (Figure 21-c). Chemical shift of 0.4 – 0.7 eV to lower binding energies has been reported for the Ag3d of AgPd compounds as well [71]. $Ag3d_{5/2}$ signal for metallic state, AgO and Ag_2O were reported in the literature as 368.2 eV, 367.4 eV and 367.8 eV, respectively [74]. Due to the close proximity of the B.E. values of the $Ag3d_{5/2}$ signal for different oxidation states of silver and the high full width at half maximum (FWHM) of the signal in Figure 21-c, it is not easy to determine the exact oxidation state of Ag in a conclusive manner, however it is clear that silver exists mostly in oxidic state. This is feasible as Ag sites can readily be synthesized after synthesis upon exposure to air under ambient conditions. Silver oxide species were reported to result in broadening in the $Ag3d_{5/2}$ signal. Therefore, it would be informative to compare FWHM value of the current $Ag3d_{5/2}$ signals with that of literature values. FWHM of the $Ag3d_{5/2}$ signal of Ag^0 was found to be 0.64 eV while that of Ag_2O was 1.00 eV

[75]. FWHM of Ag $3d_{5/2}$ species on oxidic Ag species on Ag/SiO_2 was found to be 1.8 eV [76]. Broader FWHM of 1.67 eV for the currently presented $Ag3d_{5/2}$ signal is consistent with the presence of oxidic silver species (*i.e.* Ag^{x+}).

$Pd3d_{5/2}$ signal for the PdAg sample was observed at 335.0 eV which can be attributed to metallic Pd (Figure 21-d). However, the $Pd3d_{5/2}$ signal was detected at 335.6 eV for the PdAgCr sample with a +0.6 eV chemical shift to higher B.E. values with respect to that of the PdAg catalyst. The chemical shifts of oxidic Pd^{2+} and Pd^{4+} species from the metallic Pd were reported to be +(1.1 -1.9) eV and +(2.1-3.1) eV; respectively [77]. Thus, +0.6 eV chemical shift for the $Pd3d_{5/2}$ signal in Figure 21-d can be attributed to the presence of Pd^{2+} species due to the alloying of PdAg with Cr atoms in the PdAgCr NPs. It is clear that addition of Cr lead to a significant change in the electronic structure of the active sites of the catalyst. Apparently, Cr triggers electron transfer from Pd leading to oxidized Pd species in the PdAgCr NPs. This striking difference between the electronic structure of the active sites in PdAg-MnO_x/SiO_2-NH_2 and PdAgCr-MnO_x/SiO_2-NH_2 catalysts is in perfect agreement with the differences in their corresponding FA dehydrogenation catalytic activity suggesting that alloying of PdAg with Cr leads to electron donation from the active Pd sites. As will be shown in the latter sections, this observation has also extremely significant implications on the adsorption characteristics of the catalytically active sites which will be demonstrated *via* current *in-situ* FTIR experiments. It should be noted that due to the low loadings of Cr used in the current catalyst formulations, Cr2p signal in XPS was extremely weak, excluding the possibility of further chemical analysis of Cr species.

3.3. Functional Characterization

3.3.1. Gas Phase *in-situ* FTIR Experiments

Gas phase *in-situ* FTIR spectra were collected for gaseous HCOOH, DCOOD, DCOOH and HCOOD in order to understand the vibrational features of the molecular formic acid and its deuterated counterparts in their free forms in gas phase. The assignments are straightforward and were done considering various former studies previously conducted [10], [39], [42], [78], [79]. Isotopic shifts in the vibrational features of the deuterated samples were also theoretically calculated. Since the oscillator force constant (k), is not significantly perturbed by isotopic substitution, reduced mass (μ) is the major factor affecting the vibrational frequency. There is a factor of *ca.* $1/\sqrt{2}$ difference between the vibrational frequencies of X-H and X-D (X = C, O) reduced masses, as can be seen from the reduced mass expression below;

$$\mu = \sqrt{\frac{m1 * m1}{m1 + m2}}$$

Since the increase in mass from 1 amu (H) to 2 amu (D) affects the multiplication more than the summation in the denominator, the overall change in reduced mass is predominantly governed by the lighter atom, which is either H or D, thus leading to a change in the reduced mass by a factor of *ca.* $\frac{1}{\sqrt{2}} = 0{,}707$.

Figure 22 showing gas phase HCOOH (black) and DCOOD (red) indicates that the Q branch of the ν(C=O) vibration of monomeric FA at 1774 cm^{-1}, while the corresponding feature for FA dimer is visible at around 1745 cm^{-1} [80]. The splitting in this region for α-polymer as a result of coupling in polymer/oligomer groups are explained by Sim et al. previously [9]. The H-bonding in FA species manifests itself in O-H vibrations and the vibrational frequency increases with increasing

intermolecular H-bonding 2500-3500 cm^{-1} in Figure 22 are also consistent with the former studies. [8]. 1156 cm^{-1} band appearing in all the of the isotopically labelled gaseous species can be due to the existence of D_2O in the materials [81]. Moreover, the broad band around 924-1000 cm^{-1} in DCOOD and DCOOH are associated with δ(CD) vibrations that are shifted from δ(CH) at 1364 in HCOOH (g) [82].

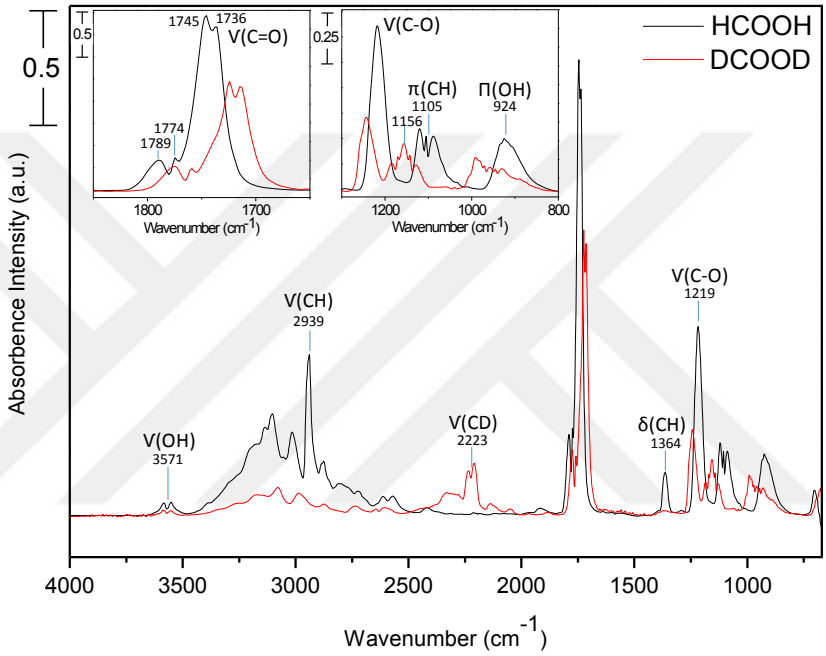

Figure 22. *In-situ* FTIR spectra of gas phase HCOOH and DCOOD obtained in the presence of 5 Torr of each species for 5 min (4 cm-1 resolution, 128 scans, 3.5 mm aperture size, 10 kHz scan rate). Insets show the detailed line shapes in various regions of the spectra.

The band in 1143 cm^{-1} for DCOOH (pink) in Figure 23 is assigned to COH bending mode that exist at 1105 cm^{-1} in FA [78]. Presence of OH group in the isotopically labelled compound in Figure 23 shows itself as a broad band around 924 cm^{-1} while presenting COH bending mode at 1143 cm^{-1}. ν(C=O) is shifted to lower frequencies due to the increased reduced mass which is inversely related to vibrational

frequency. A very similar (15 cm^{-1}) shift was observed in DCOOH as in DCOOD indicating that these shifts are mostly related to formyl (HCO/DCO) and affected very weakly by OH groups.

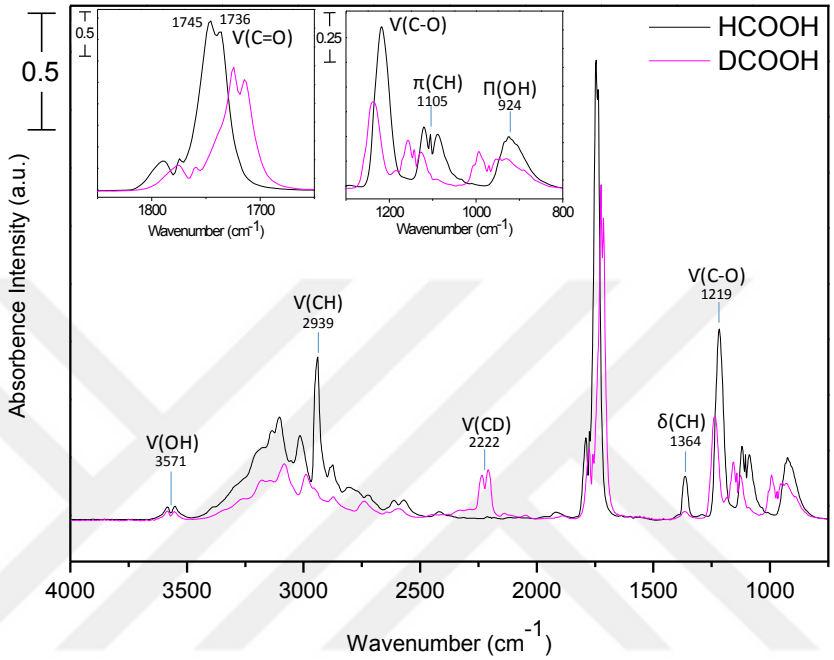

Figure 23. *In-situ* FTIR spectra of gas phase HCOOH and DCOOH in the presence of 5 Torr of each species for 5 min (4 cm^{-1} resolution, 128 scans, 3.5 mm aperture size, 10 kHz scan rate). Insets show the detailed line shapes in various regions of the spectra.

The ν(C=O) band appearing around 1730-1750 cm^{-1} in HCOOD (blue) appears at the same wavenumber with HCOOH (black) in Figure 24 confirming the effect of mass change in only formyl functionality. Since formy-H is not changed in HCOOD, C=O vibration remains the same. The lack of π(OH) vibration can be noticed in the HCOOD gas phase spectrum in Figure 24. It is clear that OD group cannot be observed in the current gas phase *in-situ* FTIR spectra due to the shift of these features outside the frequency range that can be analyzed *via* the current IR optics utilizing BaF_2 windows. The band appearing at 2301 cm^{-1} for HCOOD and at 2311 cm^{-1} for DCOOD spectra

in Figure 24 suggest the existence of ν(OD) which is shifted from the 3250-3050 cm^{-1} OH features of FA. This is consistent with the well-known fact that H-bonded OH groups appear in the region of 3650-3200 cm^{-1} [7] and these broad features can expand to lower frequencies as the extent of H-bonding increases.

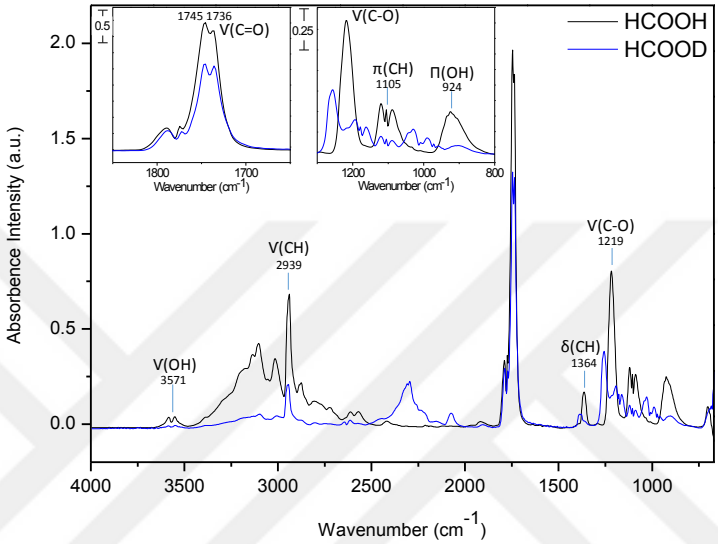

Figure 24. *In-situ* FTIR spectra of gas phase HCOOH and HCOOD in the presence of 5 Torr of each species for 5 min (4 cm^{-1} resolution, 128 scans, 3.5 mm aperture size, 10 kHz scan rate). Insets show the detailed line shapes in various regions of the spectra.

3.3.2. *In-situ* FTIR Experiments: FA Adsorption on Catalyst Surfaces

FA adsorption has been studied extensively in the literature using a variety of vibrational spectroscopic techniques on single crystal model catalyst surfaces as well as on high surface area powder catalysts comprising a very large pool of data. These literature results are summarized in Table 4 below. It should be noted that there are numerous disagreements in peak assignments in the existing literature due to broad and heavily convoluted vibrational features of FA on catalyst surfaces originating from multiple types of adsorbed FA species/surface functional groups.

	K/Cu/SiO_2 [46] **FTIR**	**Cu (110)** [44] **FTRAIR**	**Pt (111)** [42] **HREEL**	**Ni(110)** [10] **RAIR NiO**[44]	**Ag**[9] **HREEL (111) IR (110)**	**Ru (001)** [9], [41]	**SiO_2** [55] **FTIR** [80]	**Pd/SiO_2** [55] **FTIR**	**Ca-Pd diamine/ SiO_2** [55] **FTIR**	**AMO** [83]	**TiO_2** [84], [85] **ATR V–Ti oxide** [86] **FTIR**	**Pt/TiO₂**	**γ-Al_2O_3** [80]
δ (O-C=O)		787[m] 797[x]	790[f]										
δ (O-C-O)		767[b]		770[f] [10]	752 (111) 770 (110)	784[9], [41]							
δ (OH)		960[x]	980[x]										
π (CH)		1078[x]		1000[f] [10] 1040[x] [44]	1050 (110)		1147[x] [80]						1066[x]
ν (C-O)		1266[m] 1235[x]	1230[x]	1230[x] [44]			1246[x] [80]				1180[x] [86]		1202[x]
ν_S (OCO)	1355	1355	1340[f]	1345 1365[f] [10]	1351(δ) 1340(β) 1331(α) 1280(γ) (111) 1340 (110)	1361[9], [41]	1357[f,x] convoluted) [55]		1377 1353[b]		1370 [84] 1350 [85] 1250[m] 1365[b] [86]	1375	1387[f]
δ (CH)	1376	1381[m] 1388[x]		1384[f] [10] 1395[x] [44]			1390[x] [55] 1359[x] [80]			13871 364[f]	1386[85] 1375[b] [86]		1406[x] 1361[f]
ν_{aS} (COO)	1897			1600[f] [10]	1548(δ) 1580(β) 1608(γ) (111) 1640 (110)	-		1590[b]	1590[b]	1584	1573 [84] 1581 1542 [85] 1668[m] 1550[b] [86]	1554	1604[f]
ν (C=O)		1640-1670[m] 1733[x]	1640 1720[x]	1705[x] [44]			1725[x] 1791 1775[x] (R&Q) 1725[b][55] 1719[x] [80]	1725[x]	1730[x] 1700[m]	17051 600[p]	1673[x] [84] 1720[x] [86]	1679[x]	1717[x]
δ(HOC)+ ν(C-O)		2574[x]											
ν(C=O) + π (CH)		2757[x]											
ν (CH)	2776	2865[m] 2849[b] 2937[x]	2960[x] 2950[f]	2840[f] [10] 2995[x] [44]	2936-2886 (111) 2900 (110)	2930[9] 2939 [41]	2939[x] [55] 2933[x] [80]	2856[b]	2858[b]	2884	2872[f] 2938[x] [84] 2883[b] 2945[x] [86]	2872[f] 2938[x]	2925[x] 2881[f]
ν_{aS} (COO)+ δip(CH)		2945[m] 2930[b]			2840-2808 (or 2δ(CH)) (111)						2959 [84]	2952	
ν_{aS} (COO)+ ν (CH)	2692												
ν (OH)		3100[x]	2620[x]	3530[x] [44]			3064[xd] 2727 2572[xp] [55] 3738 3053[x] [80]						3733 3050[x]
δ(HOH)								1630			1650 [84] 1630 [85]	1646	
Chemisorbed CO								2082 2060 (mono), 1645 1870 (multi coord)				2057-2065, 1838 (multi)	

Table 4. Vibrational frequencies and the corresponding assignments of formic acid and formates adsorbed on various catalysts. Physisorbed FA [x], formate [f], monodentate [m], bidentate [b], polymeric FA [p], dimeric FA [d].

3.3.2.1. HCOOH, DCOOD, HCOOD and DCOOH Adsorption on fresh PdAgCr-MnO_x/SiO_2-NH_2 catalyst

PdAgCr-MnO_x/SiO_2-NH_2 catalyst was investigated for FA adsorption properties *via in-situ* FTIR using FA, HCOOD, DCOOH and DCOOD. 6 of the vibrational modes of the adsorbed molecules that are discussed in former sections are shown in Figures 25-28. It should be noted that the samples corresponding to the data in Figures 25-28 were heated to 50-100 ^oC in vacuum before the adsorption experiments in order to eliminate the water species adsorbed on the catalyst surfaces. High temperature annealing was avoided to preserve the original catalyst structure and sustain its activity. Vibrational frequency shifts for –OD and –CD were detected in their corresponding IR regions. Frequency shifts to lower wavenumbers are expected, however due to poor signal to noise (S/N) below 1250 cm^{-1}, it was not possible to detect them. This is partly due to the lattice vibrations and/or Si-O phonon modes as well as optical cut-off of the IR optics.

Comparison of the *in-situ* FTIR spectra of PdAgCr-MnO_x/SiO_2-NH_2 catalyst exposed to HCOOH and DCOOH are given in Figure 25. Disappearance of the peaks at 1385 and 1365 cm^{-1} with deuteration suggests that these modes have mostly δ(HCO) character rather than ν_{as}(OCO) stretching. Existence of a small peak at 1393 cm^{-1} in the DCOOH spectrum can be attributed to the overlap of δ(HCO) and ν_{as}(OCO). Presence of HCOOH-like minority features in the DCOOH spectrum given in Figure 25 could be due to the presence of HCOOH impurities in the original DCOOH sample or HCOOH species that are generated by H-exchange with surface -OH species. This result will be important for the assignment of the formate species in the forthcoming sections. δ(OCO) mode of most of the formates on metal surfaces are observed at 773 cm^{-1} [9]. In addition, splitting in ν(CH) in Figure 25 (black spectrum) is associated

generally with a combination band or overtone, although, it may also originate from different types of formates on the surface. Lower ν(CH) frequencies (~2902, 2827 cm^{-1}) generally indicate the presence of α and β formate species while higher frequencies of this mode (~2936, 2840 cm^{-1}) correspond to γ and δ formates [9]. The shoulder located at 1647 cm^{-1} for the HCOOH/PdAgCr-MnO_x/SiO_2-NH_2 spectrum in Figure 25 also exists in the DCOOH/PdAgCr-MnO_x/SiO_2-NH_2 spectrum, while asymmetry in lower wavenumber side of the 1647 cm^{-1} peak also indicates 1620 cm^{-1} adsorption. Figure 25 also shows that IR absorption intensities of identical exposures of FA and DCOOH are not identical and the deuterated samples lead to lower IR intensities. This can be attributed to the different IR absorption cross sections or differences in the surface coverages of adsorbates. IR absorption cross section of oscillators in transmission mode is proportional to the second power of the derivative of the dipole moment of the oscillator with respect to the distance between the atoms of the oscillator. It is feasible that the IR absorption cross-section of the deuterated samples could be lower due to the differences in the dynamic dipole moment of the C-H vs. C-D bonds. Dipole moment of an oscillator depends on charges of atoms (i.e. polarity) and the separation between the atoms. It is known that C-D bonds are slightly shorter than C-H bonds which may result in a smaller dipole moment of the C-D oscillator during vibration, which can in turn, cause a lower IR absorption cross section for the deuterated case. In addition, adsorption energy of the adsorbates and thus the surface coverages of the adsorbates could also change slightly upon deuteration which may also result in the observed decrease in the IR intensities.

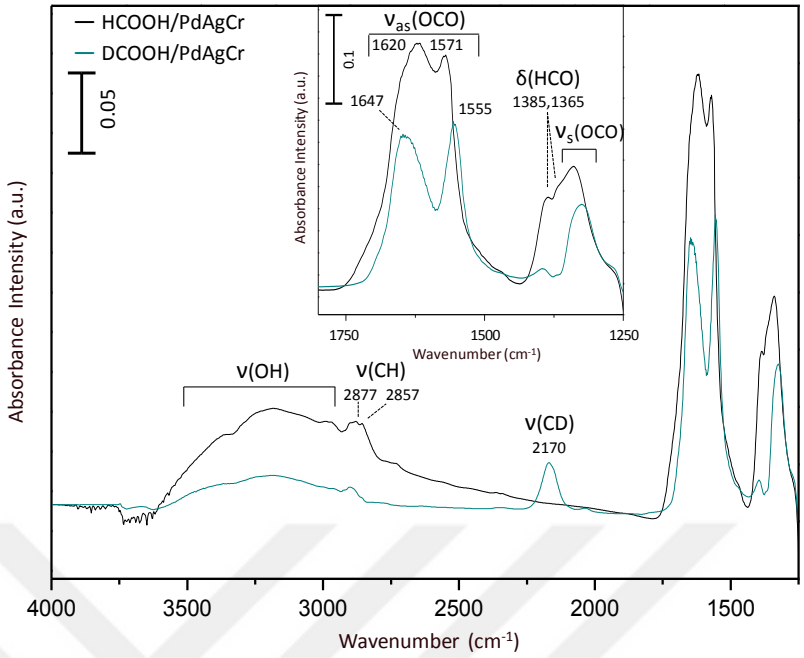

Figure 25. *In-situ* FTIR spectra and vibrational mode assignments of FA and DCOOH adsorption onto the fresh PdAgCr-MnO_x/SiO_2-NH_2 catalyst surface. HCOOH/PdAgCr-MnO_x/SiO_2-NH_2 (black), DCOOH/PdAgCr-MnO_x/SiO_2-NH_2 (cyan).

The comparison of *in-situ* FTIR spectra of fresh PdAgCr-MnO_x/SiO_2-NH_2 catalyst after FA and HCOOD adsorption on fresh surface can be found in Figure 26. The ν(OD) band around 1880 cm^{-1} appears at lower frequencies (blue) than that of FA (black). As expected, ν(CH) peak frequency at 1685 cm^{-1} remains unchanged for both cases (black and blue). δ(HCO) mode is clearly observable since both compounds have H directly bonded to C atom. Asymmetric OCO stretching around 1645-1570 cm^{-1} of HCOOD is considerably similar to HCOOH. The decrease in the absorption intensity at 3732 cm^{-1} in HCOOD/PdAgCr-MnO_x/SiO_2-NH_2 (blue) compared to HCOOH/PdAgCr-MnO_x/SiO_2-NH_2 (black) is due to the loss of the isolated surface -OH groups of SiO_2 support which start to interact with FA and/or formates via H-

bonding. This is also consistent with the broad and intense envelope between 3500-3000 cm^{-1} corresponding to H-bonded surface OH functionalities. On the other hand, higher 3200-3000 cm^{-1} absorption intensity in HCOOH/PdAgCr-MnO_x/SiO_2-NH_2 (black) than HCOOD/PdAgCr-MnO_x/SiO_2-NH_2 (blue) suggests that -NH_x groups on the support react with FA through an acid base reaction, where FA donates a proton to the surface amine groups to form formates and protonated ammonium cations on the surface [55], [80]. The broad OH band cannot be attributed to formates as they have no OH groups, however, another source of this band could be physisorbed/chemisorbed FA. Molecularly adsorbed FA on alumina and silica surfaces results in a similar broad OH band [80].

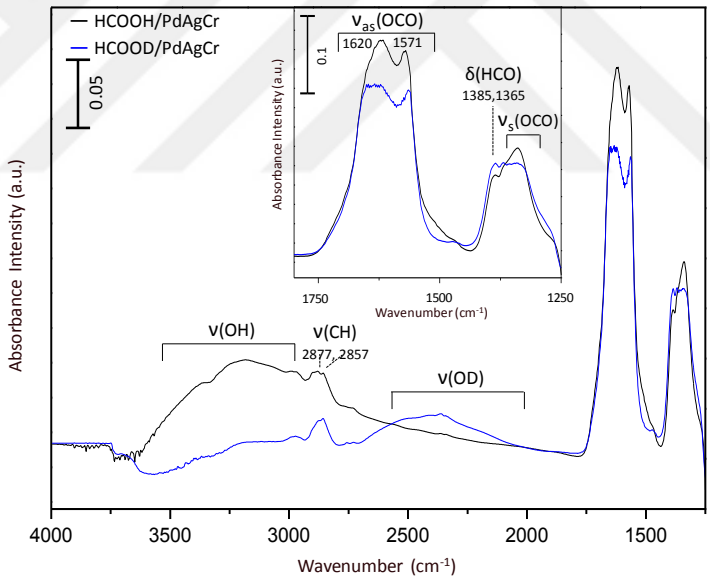

Figure 26. *In-situ* FTIR spectra and vibrational mode assignments of FA and HCOOD adsorption onto the fresh PdAgCr-MnOx/SiO2-NH2 catalyst surface. HCOOH/PdAgCr-MnOx/SiO2-NH2 (black), HCOOD/PdAgCr-MnOx/SiO2-NH2 (blue).

Finally, *in-situ* FTIR spectra for FA and DCOOD adsorption on fresh PdAgCr-MnO_x/SiO_2-NH_2 catalyst are shown in Figure 27. 700-800 cm^{-1} shift of ν(OH) band as

well as ν(CH) can be followed by ν(OD) and ν(CD) bands in DCOOD/PdAgCr-MnO_x/SiO_2-NH_2 (red) spectra. Two different δ(HCO) features observed for FA (black) adsorption around 1385 and 1365 cm^{-1} vanished for DCOOD (red) adsorption since they shift to lower wavenumbers approximately by 400 cm^{-1} due to the isotope effect. The peak around 1620 cm^{-1} in HCOOH also shifted to slightly lower frequency in DCOOD due to the increased reduced mass, while the shoulder at 1642 cm^{-1} remained intact.

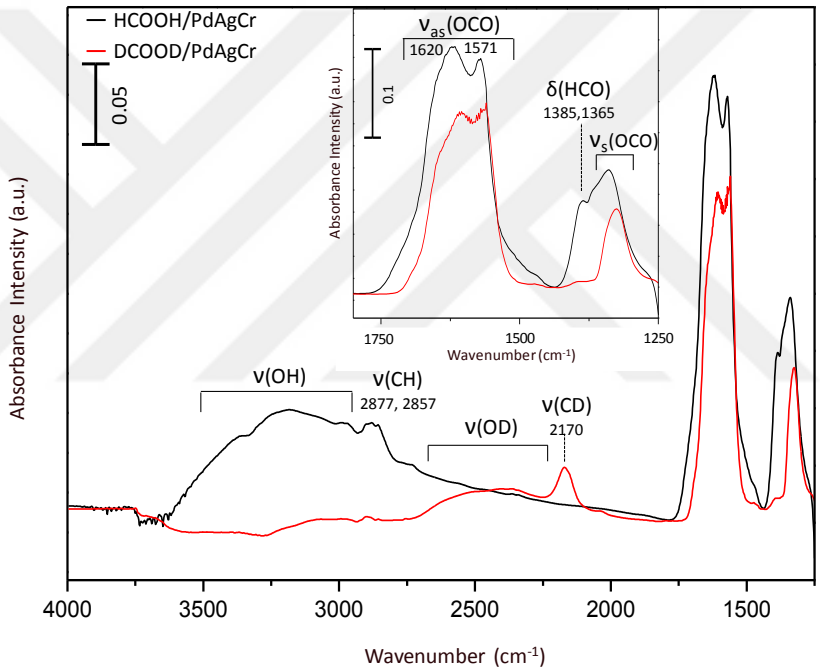

Figure 27. *In-situ* FTIR spectra and related assignments of PdAgCr-MnO_x/SiO_2-NH_2 catalyst after FA and DCOOD adsorption onto the fresh surface. HCOOH/PdAgCr-MnO_x/SiO_2-NH_2 (black), DCOOD/PdAgCr-MnO_x/SiO_2-NH_2 (red).

A detailed comparison of the asymmetric OCO stretching mode for FA and other with isotopically labelled species were investigated in Figure 28-a. General features of these spectra are similar while there exist minor differences in peak

intensities and small shifts to lower wavenumbers due to the higher mass of deuterium. δ(HCO) peaks at 1385, 1365 cm^{-1} for HCOOH/PdAgCr-MnO_x/SiO_2-NH_2 (black) and HCOOD/PdAgCr-MnO_x/SiO_2-NH_2 (blue) samples disappeared in DCOOH/PdAgCr-MnO_x/SiO_2-NH_2 (cyan) and DCOOD/PdAgCr-MnO_x/SiO_2-NH_2 (red) materials implying the presence of at least two different types of formates on PdAgCr-MnO_x/SiO_2-NH_2. The disappearance of these signals of two different formates is due to the shift of δ(DCO) peaks to the lower wavenumbers in DCOOH (cyan) and DCOOD (red) spectra.

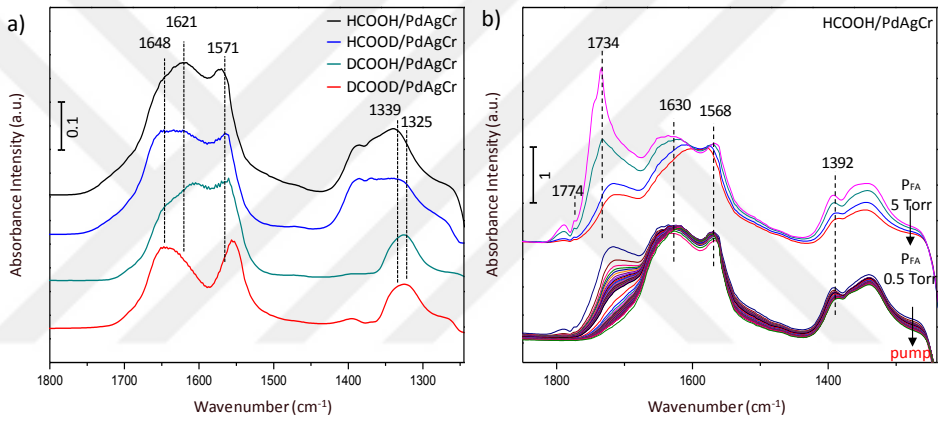

Figure 28. (a) *In-situ* FTIR spectra of PdAgCr-MnO_x/SiO_2-NH_2 catalyst in the formate region after the adsorption of HCOOH (black), HCOOD (blue), DCOOH (cyan), and DCOOD (red) (b) *In-situ* FTIR spectra of FA adsorption on PdAgCr-MnO_x/SiO_2-NH_2 catalyst with decreasing gas pressure from 5 Torr to 10^{-6} Torr.

In order to differentiate between the molecular FA species and formates on the catalyst surface, changes in the *in-situ* FTIR spectra were monitored as a function of decreasing gas pressure (Figure 28-b). 1774 cm^{-1} corresponds to the characteristic gas phase FA ν(C=O) vibration, while 1734 cm^{-1} can be attributed to dimeric FA, α-oligomer or β-oligomer. Figure 28-b shows that removal of gas phase FA could be readily achieved by pumping the gas out of the system to very low pressures.

Physisorbed/chemisorbed FA with vibrational features similar to gas phase FA could be observed around 1774 and 1734 cm^{-1} which could also be readily eliminated after evacuation. Hence, the weak and broad shoulder in the higher frequency side of the formate band around 1700 cm^{-1} in Figure 28-b can be ascribed to chemisorbed FA. This feature can also be correlated with the strong band in the OH stretching (*i.e.* 3200-3500 cm^{-1}) region. 1630-1640 cm^{-1} bands were assigned to adsorbed molecular FA on Pd (111) by Zheng et al. [87]. On the other hand, peak at 1660 cm^{-1} was assigned to monodentate formate on Pd (100) with a symmetric stretch at 1340 cm^{-1} [87]. Monodentate and bidentate formates on Ag (110) surface were reported in the past with vibrational features at 1640 cm^{-1} 1570 cm^{-1}, respectively. On the other hand, monodentate formate on Pt (111) was observed to yield a signal at 1620 cm^{-1} [38]. On Ca-doped Pd-diammine/SiO_2 catalysts, bidentate and monodentate formates were observed at 1590 cm^{-1} and at 1700 cm^{-1} ; respectively [55]. It is apparent that introduction of MnO_x domains lead to a decrease in the vibrational frequencies of these differently oriented formates.

Figure 29 shows the temperature dependence of the vibrational features on the PdAgCr-MnO_x/SiO_2-NH_2 catalyst surface after FA saturation at RT followed by evacuation at RT. Removal of the formates as a function of annealing in vacuum starts with the initial elimination of the δ-formate species followed by the disappearance of the γ, β and α-formates, respectively [9]. α-Formates with the bridging adsorption geometry (1571 cm^{-1}) seems to have the strongest attachment to the surface consistent with the former studies in the literature [55]. Figure 29 shows that with increasing temperature, the peak at 1647 cm^{-1} vanished and the band at 1620 cm^{-1} red shifted. These observation suggests the desorption/decomposition of monodentates leaving bidentate formates as the predominant species on the surface. The splits between

ν_{as}(OCO) at 1650-1570 cm^{-1} and ν_s(OCO) 1350-1300 cm^{-1} are also in agreement with the discussion given above regarding the types of formates as a function of temperature. The new peaks occurring *ca.* at 1583 cm^{-1} (ν_{as}) and 2170 cm^{-1} (ν_s) at elevated temperatures reveals the formation of bidentate carbonates possibly generated due to the decomposition of the alkyl functionalities in the APTS groups and their subsequent oxidation with the surface oxygen species of MnO_x [7]. The asymmetry of the 1583 cm^{-1} peak in Figure 29 might also be related to the formates as well. The small peak located at 1492 cm^{-1} becoming discernible particularly at high temperatures is associated with HCO which eventually leads to the formation of CO [88]. Relatively small intensity of this peak may suggest that the reaction does not follow the dehydration mechanism and CO formation is quite limited.

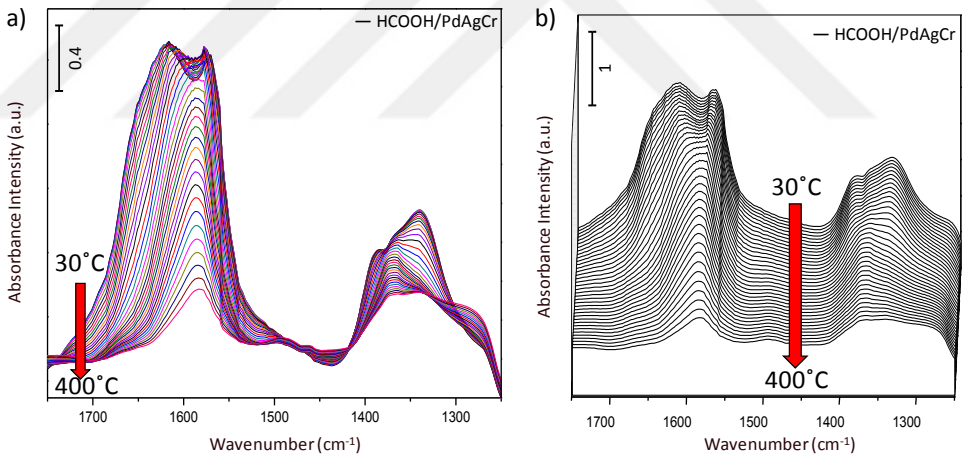

Figure 29. *In-situ* FTIR spectra acquired after saturation of the fresh PdAgCr-MnO_x/SiO_2-NH_2 catalyst with FA at RT followed by evacuation at RT and subsequent heating in vacuum. Spectra were obtained in every 10 ^oC rise in temperature. Each spectrum was obtained at the depicted catalyst temperatures in vacuum: (a) line plot (b) 3-D representation.

3.3.3. *In-situ* FTIR Experiments: CO Adsorption

In-situ FTIR spectra corresponding to the interaction of CO and the synthesized catalysts at room temperature is shown in a systematical way in Figure 30. The signals at 1588 and 1358 cm^{-1} correspond to the typical carbonate (CO_3^{-2}) features [7]. Absence of carbonate formation on the SiO_2 support material upon CO (g) introduction is consistent with the highly acidic nature of this surface (Figure 30-a).

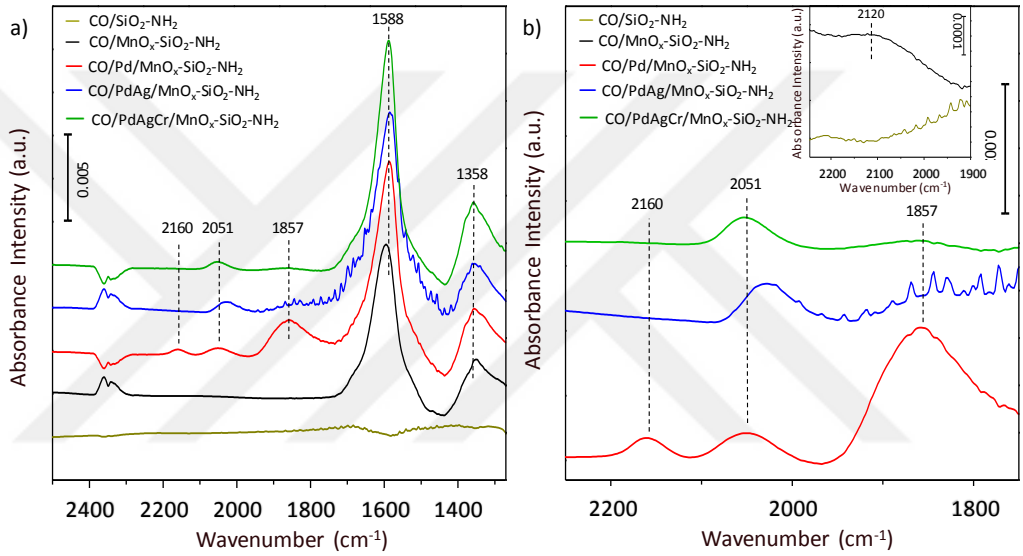

Figure 30. *In-situ* FTIR spectra of MnO_x/SiO_2-NH_2 and its functionalized derivatives after the exposure of 20 Torr CO(g) at RT for 65 min. **(a)** Global representation of the spectra revealing gas phase CO_2 (g), carbonyl, and carbonate features, **(b)** Close up of the carbonyl region. Inset in part b emphasizes the absence of carbonyl species on SiO_2-NH_2 and very weak adsorption of carbonyls on PdAgCr-MnO_x/SiO_2-NH_2.

It is worth mentioning that we have also performed and extremely comprehensive set of experiments on unsupported versions of the investigated catalysts in the absence of silica and by changing the morphology and the oxidation state of the MnO_x domains. However, in most of these catalysts, MnO_x domains were

chemically not stable in FA solution due to leaching. Furthermore, the limited number catalysts which survived in the FA solution did not yield significant catalytic activity. In addition, their very low IR transmissivity prevented their detailed analysis with *in-situ* FTIR spectroscopy due to the extremely small S/N of the FTIR corresponding spectra. Figure 30 shows that CO adsorption on MnO_x/SiO_2-NH_2 leads to monodentate ($\nu_{as}(COO^-)$ 1530-1300, $\nu_s(COO^-)$ 1370-1300) and bidentate/bridging (ν(C=O) 1670-1620, $\nu_{as}(COO^-)$ 1270-1250) carbonyls possibly coordinating to the Lewis basic O^{-2} and O_2^{-2} centers [7], [89]. The presence of surface carbonates with different geometries after CO (g) adsorption and subsequent evacuation demonstrates the high stability of these strongly adsorbed species. This finding clearly reveal that MnO_x phase adsorbs the poisonous CO (g) produced in the FA dehydrogenation reaction in the form of carbonates and hinders and/or suppresses the poisoning of the active sites. A closer look at the carbonyl species is given in Figure 30-b. The inset displays a very weak band around 2120 cm^{-1} for the MnO_x/SiO_2-NH_2 monometallic material revealing the very limited extent of carbonyl presence on MnO_x sites upon CO (g) adsorption.

The red spectrum obtained by CO (g) adsorption on Pd-MnO_x/SiO_2-NH_2 shows strong carbonyl peaks (2200-1700 cm^{-1}) in addition to the carbonate species on the surface. The adsorption geometries of the carbonyls present on the Pd/PdO_x active sites can be determined from their C-O vibrational frequencies. An IR vibrational frequency higher than gas phase CO (g) characteristically located at 2143 cm^{-1} indicates an electron density transfer from the antibonding molecular orbital of CO (g) to the Pd sites as well as a concomitant increase in the bond order and force constant of the CO oscillator. The carbonyl signal at 2160 cm^{-1} can be assigned to linear/atop CO adsorption on oxidized Pd species, while 2041 cm^{-1} peak is associated with bridging carbonyl species that are adsorbed on Pd/PdO_x facets through two different

Pd atoms/ions. The low-frequency CO feature at *ca.* 1857 cm^{-1} in Figure 30 corresponds to three-fold/hollow carbonyls coordinated to the oxidized Pd surface *via* three separate Pd atoms/ions simultaneously. Three-fold adsorption geometry is typically favored on extended flat surfaces and terrace sites on polyhedral NPs. Presence of polyhedral Pd/PdO_x NPs is also consistent with the current HRTEM results presented above (Figure 19). Additionally, the signals of surface carbonates were stronger for $Pd\text{-}MnO_x/SiO_2\text{-}NH_2$ as compared to $MnO_x/SiO_2\text{-}NH_2$ sample (Figure 31-b), while there is no carbonate formation on $SiO_2\text{-}NH_2$ (Figure 31-a). This observation points to the fact that CO (g) can efficiently adsorb on Pd/PdO_x followed by their subsequent spill-over onto MnO_x domains. In other words, presence of MnO_x species offer an alternative storage domain for CO, preventing its accumulation on Pd/PdO_x centers and poisoning of the active sites. Along these lines, MnO_x domains seem to serve as sacrificial sites which can suppress the CO poisoning. It is also important to mention that carbonate species in all of the MnO_x-containing catalysts are rather similar which is in agreement with the argument that carbonates are stored almost exclusively on the MnO_x domains.

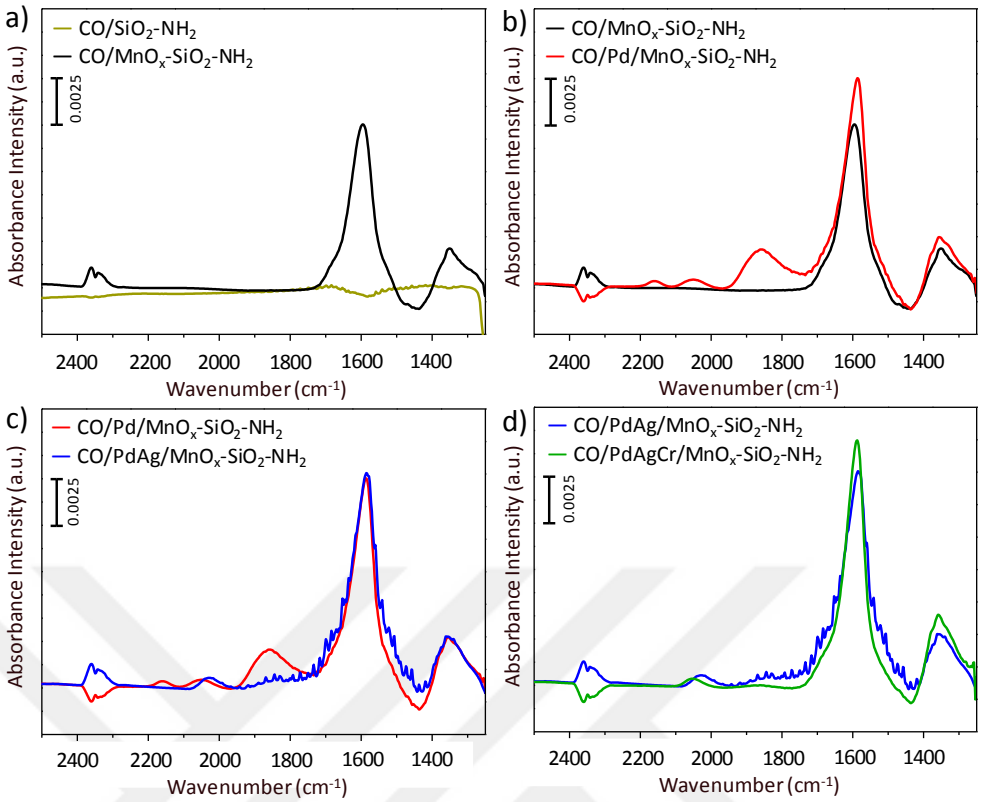

Figure 31. *In-situ* FTIR spectra of investigated catalysts after exposure of 20 Torr CO(g) for 65 min at RT. (a) Comparison of absorbance intensities of SiO_2-NH_2 and MnO_x/SiO_2-NH_2, (b) MnO_x/SiO_2-NH_2 and Pd-MnO_x/SiO_2-NH_2, (c) Pd-MnO_x/SiO_2-NH_2 and PdAg-MnO_x/SiO_2-NH_2, (d) PdAg-MnO_x/SiO_2-NH_2 and PdAgCr-MnO_x/SiO_2-NH_2 after CO(g) adsorption.

Ag metal was used to improve the CO poisoning tolerance of the currently investigated catalytic materials. CO(g) adsorption on Ag leads to a vibrational feature at >2169 cm^{-1} for alumina [90] and silica [91], [92] supported materials. Lack of such Ag-CO peaks in the spectra given in Figures 31-c and 31-d implies that CO adsorbs either very weakly or does not adsorb at all on Ag sites. Disappearance of the linearly bonded CO species (Figure 30-a and 31-c and 31-d) and presence of highly coordinated bridging and 3-fold carbonates are consistent with the weakening of the interaction between CO and the active sites in the presence of Ag species. It should be

noted that adsorption energy (E_{ads}) of the carbonyls on many transition metals increase in the following order: E_{ads} (linear CO) < E_{ads} (bridging CO) < E_{ads} (3-fold CO). Thus, disappearance of the linear carbonyls is a clear indication of the decreasing affinity of the active sites towards carbonyls in the presence of Ag species which are alloying with Pd atoms in the multimetallic NP active sites. The vibrational frequency shift in the bridging carbonyls upon introduction of Ag species can be attributed to the electronic effect of Ag on Pd sites altering the d-band structure of Pd sites in NPs; and weakening the adsorption energy of CO. Additionally, the red shift in carbonyl IR frequencies in PdAg-MnO_x/SiO_2-NH_2 with respect to Pd-MnO_x/SiO_2-NH_2 also validates the lower oxidation state (*i.e.* more metallic-like character) of Pd in PdAg-MnO_x/SiO_2-NH_2 catalyst compared to other materials (Figures 30-b and 31-c). On the other hand, it is apparent that incorporation of Cr clearly leads to a further modification of the electronic structure of the PdAgCr alloy NPs, leading to slight blue shift in carbonyl IR frequencies with respect to that of the PdAg system (Figure 30-b and Figure 31-d). This is in perfect agreement with the current XPS results (Figure 21) suggesting that the oxidation state of Pd is lower for PdAg while it is higher for PdAgCr catalysts. Figure 31-c illustrates that the intensity of the three-fold carbonyl adsorption decreased drastically upon Ag addition to the monometallic Pd active sites. Decreasing 3-fold CO to bridging CO ratio in PdAg-MnO_x/SiO_2-NH_2 compared to Pd-MnO_x/SiO_2-NH_2 also suggests that Ag alloys with Pd rather than forming separate domains. This observation is also in very good coherence with the current STEM-EDX measurements (Figure 20) suggesting the presence of multi-metallic alloy NP. Furthermore, as a direct consequence of alloying, simultaneous presence of Ag and Cr species in the trimetallic system leads to a further attenuation of the 3-fold CO signal intensity (Figure 30 and 31-d). This can be explained by the decreased concentration

of Pd-Pd-Pd neighbors in the NPs due to the distribution of Ag and Cr atoms in between Pd neighbors. Since 3-fold coordinated carbonyls result in more severe poisoning due to their higher adsorption energy, decreasing surface coverage of 3-fold CO species imply enhanced CO tolerance for the trimetallic PdAgCr NPs.

A previous study in the literature reported that CO (g) adsorbed on Cr/SiO_2 exhibited IR features at 2184 cm^{-1} for Cr^{+2} sites and 2212 cm^{-1} for Cr^{+3} sites, whose frequencies may vary further depending on temperature, catalyst pretreatment and CO coverage [93]. Another study reported CO vibrational features at 2170 and 2132 cm^{-1} on $Cr_2O_3(0001)/Cr$ (110) at 90K [94]. Calculated CO stretching frequencies on Cr (110) surface strongly depends on the orientation of the C-O oscillator with respect to the surface. Experimental results supported the calculated CO arrangements indicating that, CO lying parallel to the surface of Cr(110) yielded IR signature at 1330 cm^{-1} while almost perpendicular CO orientation led to IR signals at 1865 and 1975 cm^{-1} [95]. Although, the lack of CO band at 1975 cm^{-1} on $PdAgCr\text{-}MnO_x/SiO_2\text{-}NH_2$ probably indicates that CO does not primarily adsorb on Cr sites of the catalyst.

The increase in the of carbonate population and decrease in the carbonyl species on the $PdAgCr\text{-}MnO_x/SiO_2\text{-}NH_2$ catalyst suggest that this particular catalyst has superior CO poisoning tolerance compared to all of the other currently investigated catalysts. As mentioned earlier, this can be explained by two different types of enhancements introduced by Cr sites in the trimetallic PdAgCr alloy NPs, namely the electronic modification of the d-band structure of the active sites and the geometric modification of the adsorption sites resulting in the destruction of the all-Pd 3-fold adsorption sites.

3.3.3.1. *In-situ* FTIR Experiments: FA Adsorption on CO poisoned catalysts

FA adsorption capabilities of the synthesized catalysts after CO (g) poisoning were also investigated in a comparative manner using *in-situ* FTIR (Figure 32).

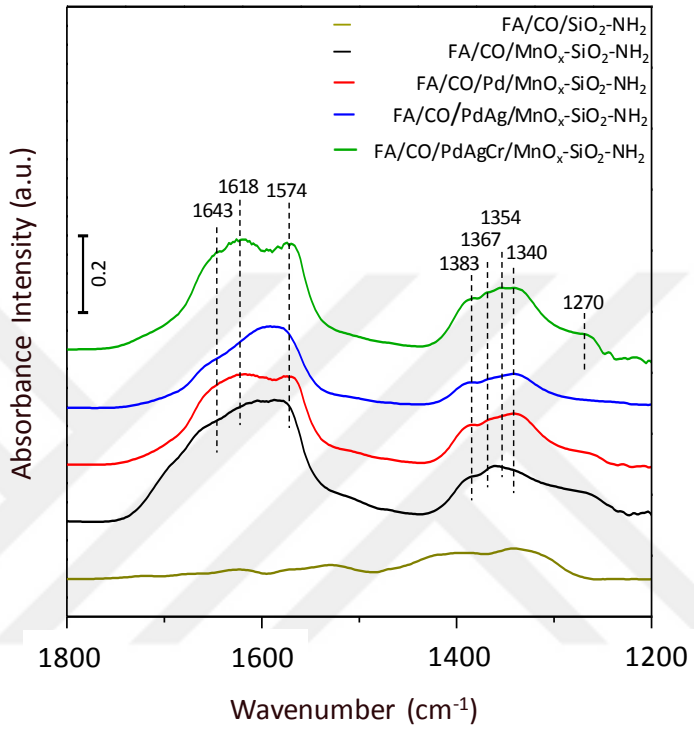

Figure 32. *In-situ* FTIR spectra for FA adsorption (5 Torr FA (g) at RT) on CO(g)-poisoned catalysts: SiO_2-NH_2 (yellow), MnO_x/SiO_2-NH_2 (black), Pd-MnO_x/SiO_2-NH_2 (red), PdAg-MnO_x/SiO_2-NH_2 (blue) and PdAgCr-MnO_x/SiO_2-NH_2 (green).

Catalytic FA dehydrogenation requires deprotonation of FA and formation of formate species to begin H_2 (g) production. However, the production of CO (g) will affect the binding of FA to the active sites of the catalyst. Thus, in the current work, the influence of CO poisoning on consequent FA adsorption was also investigated. *In-situ* FTIR spectra of FA (g) shown in Figure 28-b is extremely informative for distinguishing physisorbed molecular FA features from chemisorbed formate. Figure 32 shows typical ν_{as}(OCO) and ν_s(OCO) vibrations of bidentate formate located in the

range of 1610-1530 cm^{-1} and 1360-1260 cm^{-1}, respectively [9].

Figure 32 suggests that FA does not dissociate on the CO-poisoned SiO_2-NH_2 surface to a great extent and/or the formates generated by the dissociation of FA do not efficiently adsorb on silica. Similar results were also reported in earlier reports in the literature [7]. In the presence of MnO_x domains, formate species become visible. This critical observation implies that MnO_x domains have a vital role in the initiation and progress of the reaction.

Estimated $\nu_{as}(COO^-)$ - $\nu_s(COO^-)$ difference for monodentate γ-formate adsorption configuration is >250-300 cm^{-1} (328 cm^{-1}) [9] while the difference gets smaller for bidentate bridging (∼200) arrangements [7], [9], [83], [96]. Frequency difference of 238 cm^{-1} indicates the formation of bidentate formates on MnO_x.

According to Durand et al. [83], presence of ν_s(CH) splitting at 2840 and 2910 cm^{-1} shows that formates can exist in more than two distinct orientations on the surface. Existence of multiple adsorption orientations might also manifest itself as the observation of broad ν_s(OCO) and ν_{as}(OCO) bands. *In-situ FTIR* experiments that are done with deuterated FA reagents revealed that 1383 and 1367cm^{-1} peaks were due to ν(CH) bands of formates on the surface. Presence of 3 different formate species were estimated by the deconvolution of the formate peaks, however, such an analysis is not completely conclusive. The separation of asymmetric and symmetric stretching frequencies suggests the existence of α-formate, β-formate and δ-formate species that are dependent on the surface coverages.

MnO_x/SiO_2-NH_2 catalyst was advantageous in terms of increased CO tolerance (i.e. lack of poisoning surface carbonyl species). Although it is available for formate adsorption, it does not possess any active sites for C-H activation (Figure 2). Pd is critical for the dehydrogenation reaction to proceed (Figure 15). Since Pd-MnO_x/SiO_2-

NH_2 catalyst was previously poisoned by CO (g) before FA adsorption, the active sites were partially blocked by monodentate, bidentate and 3-fold carbonyls (Figure 30-b). The active metal poisoning result in fewer adsorbed formates on the surface (Figure 33-b). The similarity in types of adsorbed formate between those two catalysts can also be noticed. Ag is used to weaken CO (g) adsorption by preventing CO (g) poisoning of the surface. Higher tolerance towards CO (g) leads to increased number of open sites for FA adsorption. However, as is discussed in Chapter 1, Pd particles are diluted by Ag metal as it forms PdAg alloy and monodentate formate adsorption attenuates. Addition of chromium in PdAgCr-MnO_x/SiO_2-NH_2 (Figure 33-d, green) leads to the regeneration of 1618 cm^{-1} monodentate formate, points that Cr changes the electronic structure of the catalyst as it is claimed by the XPS result showing higher oxidation state of Pd. The comparison of the FA/formate absorbance intensities of all materials is given in Figure 33. Greater amount of formates on PdAgCr can be responsible for higher activity of the catalyst. Increase in the monodentate formate adsorption may have more significant effect because of their lower adsorption strength. Formates that are more strongly adsorbed on the surface such as bridging formates may have a moderate impact on the reaction.

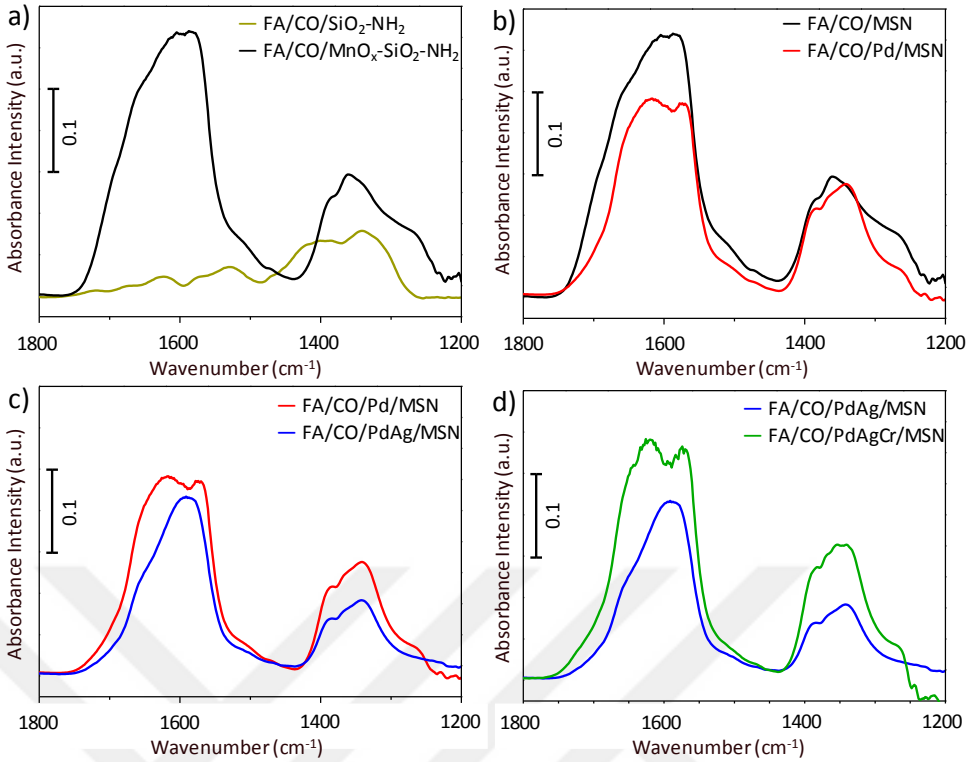

Figure 33. Comparison of *in-situ* FTIR spectra of FA adsorption on CO (g) poisoned catalsyts with 5 Torr FA (g). (a) SiO2-NH2 (yellow) and MnOx/SiO2-NH2 (black), (b) MnOx/SiO2-NH2 (black) and Pd-MnOx/SiO2-NH2 (MSN) (red), (c) Pd-MnOx/SiO2-NH2 (red) and PdAg-MnOx/SiO2-NH2 (blue), (d) PdAg-MnOx/SiO2-NH2 (blue) and PdAgCr-MnOx/SiO2-NH2 (green).

CO_2 production can proceed from activation of O-H bond forming $HCOO^-$ and/or through C-H activation forming COOH. Although formate is achieved more easily compared to COOH, energy required for the decomposition of formate is higher. Peaks associated with COOH are 3596, 1653, 1218 cm^{-1} are not observed in the FTIR spectra which can indicate the HCOO route being favored [88]. Moreover, oxides on the surface can facilitate by attracting H in both routes producing CO_2 more readily. PdAgCr-MnO_x/SiO_2-NH_2 surface having Pd active sites with higher oxidation state can result in higher reactivity.

CHAPTER 4

CONCLUSION

In this work, MnO_x/SiO_2-NH_2, Pd-MnO_x/SiO_2-NH_2, PdAg-MnO_x/SiO_2-NH_2 and PdAgCr-MnO_x/SiO_2-NH_2 materials were synthesized and characterized by XRD, Raman, BET, TEM, HRTEM, STEM/EDX, HAADF/STEM, ICP-OES, NAP-XPS and in-situ FTIR analysis. Activity of the synthesized materials were also measured in additive-free Formic acid dehydrogenation at room temperature. CO poisoning tolerance and formic acid adsorption characteristics were investigated *via in-situ* FTIR in order to understand the formic acid reaction mechanism. Some of the significant findings summarized as follows;

- Among all of the investigated monometallic catalysts, Pd was the only active metal.
- The activity of the Pd catalyst increased around 5 times higher after MnO_x promotion.
- $Pd_{0.55}Ag_{0.25}Cr_{0.20}$-$MnO_x/SiO_2$-$NH_2$ trimetallic catalyst had an outstanding activity with a TOF of 585 h^{-1} which is one of the highest in the literature.
- The crystal structure analysis with XRD revealed the metallic and oxidic states of the active metals with small loadings and relatively disordered MnO_x and SiO_2 particles. Vibrational structure analysis via Raman also demonstrated MnO_x species and partially oxidized Pd, Ag and Cr nanoparticles.
- Average particle size of the active trimetallic PdAgCr nanoparticles was found to be 3.7 with ± 0.9 nm indicating a monodisperse distribution of the nanoparticles. Presence of individual alloy NPs separate from MnO_x NPs on

APTS/SiO_2 were shown by STEM-EDX measurements.

- Influence of Cr is demonstrated using NAP-XPS by the triggered electron transfer of Pd leading to Pd^{2+} species on PdAgCr-MnO_x/SiO_2-NH_2 that is also in perfect agreement with the differences in their corresponding CO adsorption vibrational frequencies and FA dehydrogenation catalytic activity.
- Monomeric as well as dimeric FA were detected in gas phase FTIR experiments. *In-situ* FTIR studies were performed with isotopically labelled FA species. Monodentate and bidentate adsorbed formates as well as possibly chemisorbed formic acid were detected on PdAgCr-MnO_x/SiO_2-NH_2 catalyst surface. Easily released monodentate formates and very stable bidentate formates with a contribution of carbonates were detected as a function of temperature.
- CO adsorbed in the form of carbonates on MnO_x, as opposed to carbonyls. MnO_x domains appeared to be functioning as sacrificial sites preventing catalytic poisoning of the active metal sites by CO.
- Pd metal active sites were poisoned by adsorbed monodentate, bidentate, and 3-fold carbonyl species. Increase in carbonates suggested the CO spillover from NPs to MnOx domains.
- Incorporation of Ag weakened the adsorption strength and lessened the amount of carbonyls on Pd NPs on the surface. CO poisoning tolerance of PdAgCr catalyst is further increased by the co-presence of Ag and Cr.
- Poisoned Pd sites affected the amount of adsorbed formates. Inclusion of Ag changed the adsorption characteristics of formates.
- Cr addition resulted in higher amount of adsorbed formates since active sites

are not poisoned by CO which can explain the remarkable activity of the catalyst.

- Ultimately, a new, superior catalyst with high CO tolerance and outstanding activity that can produce pure H_2 and CO_2 from formic acid without any additives was achieved at room temperature with trimetallic PdAgCr active nanoparticles dispersed on MnO_x/SiO_2-NH_2 support.

BIBLIOGRAPHY

[1] P. P. Edwards, V. L. Kuznetsov, W. I. F. David, and N. P. Brandon, "Hydrogen and fuel cells: Towards a sustainable energy future," *Energy Policy*, vol. 36, no. 12, pp. 4356–4362, 2008.

[2] K. Mori, M. Dojo, and H. Yamashita, "Pd and Pd-Ag Nanoparticles within a Macroreticular Basic Resin : An Efficient Catalyst for Hydrogen Production from Formic Acid Decomposition," *ACS Catal.*, vol. 3, pp. 1114–1119, 2013.

[3] A. Bulut, M. Yurderi, Y. Karatas, M. Zahmakiran, H. Kivrak, M. Gulcan, and M. Kaya, "Pd-MnOx nanoparticles dispersed on amine-grafted silica: Highly efficient nanocatalyst for hydrogen production from additive-free dehydrogenation of formic acid under mild conditions," *Appl. Catal. B Environ.*, vol. 164, pp. 324–333, 2015.

[4] J. F. Ganghoffer, "Thermodynamics of Surface Growth with Application to Bone Remodeling." *Thermodynamics - Interaction Studies-Solids, Liquids and Gases*, 2011.

[5] P. Saxena and N. Thirupathi, "Reactions of Cd (OAc)2 2H2O with variously substituted pyridines. Efforts to unravel the factors that determine structure / nuclearity of the products," *Polyhedron*, vol. 98, pp. 238–250, 2015.

[6] K. Tedsree, T. Li, S. Jones, C. W. A. Chan, K. M. K. Yu, P. A. J. Bagot, E. A. Marquis, G. D. W. Smith, and S. C. E. Tsang, "Hydrogen production from formic acid decomposition at room temperature using a Ag-Pd core-shell nanocatalyst," *Nat. Nanotechnol.*, vol. 6, no. 5, pp. 302–307, 2011.

[7] A. Davydov, *Molecular Spectroscopy of Oxide Catalyst Surfaces*. Wiley-VCH Verlag GmbH & Co. KGaA, 2003.

[8] M. Freytes, D. Hurtmans, S. Kassi, J. Li, J. Vander Auwera, A. Campargue, and M. Herman, "Overtone spectroscopy of formic acid," vol. 283, pp. 47–61, 2002.

[9] W. S. Sim, P. Gardner, and D. a King, "Multiple bonding configurations of adsorbed formate on Ag{111}," *J. Phys. Chem.*, vol. 100, no. 30, pp. 12509–12516, 1996.

[10] S. Haq, J. G. Love, H. E. Sanders, and D. A. King, "Adsorption and decomposition of formic acid on Ni {110}," *Surf. Sci.*, vol. 325, pp. 230–242, 1995.

[11] E. Kayhan, "Structure and NOx uptake properties of Fe-Ba/Al2O3 as a model NOx storage material," no. x, pp. 1–92, 2009.

[12] A. Bulut, M. Yurderi, Y. Karatas, Z. Say, H. Kivrak, M. Kaya, M. Gulcan, E. Ozensoy, and M. Zahmakiran, "MnO x -Promoted PdAg Alloy Nanoparticles for the Additive-Free Dehydrogenation of Formic Acid at Room Temperature," *ACS Catal.*, vol. 5, no. 10, pp. 6099–6110, Oct. 2015.

[13] J. Eppinger and K.-W. Huang, "Formic Acid as a Hydrogen Energy Carrier," *ACS Energy Lett.*, vol. 2, no. 1, pp. 188–195, 2017.

[14] K. V. Kordesch and G. R. Simader, "Environmental Impact of Fuel Cell Technology," *Chem. Rev.*, vol. 95, no. 1, pp. 191–207, 1995.

[15] J. E. Mason, “World energy analysis : H2 now or later ?,” *Energy Policy*, vol. 35, pp. 1315–1329, 2007.

[16] M. Conte and M. Ronchetti, *ENERGY | Hydrogen Economy*, no. August. Elsevier Inc., 2009.

[17] J. A. Turner, “A Realizable Renewable Energy Future,” *Science (80-.).*, vol. 285, no. 5428, pp. 687–689, 1999.

[18] A. Züttel, “Hydrogen storage methods,” *Naturwissenschaften*, vol. 91, no. 4, pp. 157–172, 2004.

[19] G. W. Crabtree, M. S. Dresselhaus, and M. V. Buchanan, “The Hydrogen Economy,” *Phys. Today*, vol. 57, no. 12, pp. 39–44, 2004.

[20] D. J. Durbin and C. Malardier-Jugroot, “Review of hydrogen storage techniques for on board vehicle applications,” *Int. J. Hydrogen Energy*, vol. 38, no. 34, pp. 14595–14617, 2013.

[21] B. Sakintuna, F. Lamari-Darkrim, and M. Hirscher, “Metal hydride materials for solid hydrogen storage: A review,” *Int. J. Hydrogen Energy*, vol. 32, no. 9, pp. 1121–1140, 2007.

[22] S. Enthaler, J. von Langermann, and T. Schmidt, “Carbon dioxide and formic acid-the couple for environmental-friendly hydrogen storage?,” *Energy Environ. Sci.*, vol. 3, no. 9, p. 1207, 2010.

[23] J. Yun, F. Jin, A. Kishita, K. Tohji, and H. Enomoto, “Formic acid production from carbohydrates biomass by hydrothermal reaction,” *J. Phys. Conf. Ser.*, vol. 215, p. 12126, 2010.

[24] M. Nielsen, A. Kammer, D. Cozzula, H. Junge, S. Gladiali, and M. Beller, “Efficient Hydrogen Production from Alcohols under Mild Reaction Conditions,” pp. 9593–9597, 2011.

[25] M. B. A. Boddien, D. Mellman, F. Gartner, R. Jackstell, H. Junge, P. J. Dyson, G. Laurenczy, R. Ludwig, “Efficient Dehydrogenation of Formic,” vol. 333, no. September, pp. 1733–1737, 2011.

[26] S. Ogo, R. Kabe, H. Hayashi, and S. Fukuzumi, “Mechanistic investigation of CO 2 hydrogenation by Ru (II) and Ir (III) aqua complexes under acidic conditions : two catalytic systems differing in the nature of the rate determining step†,” *Dalt. Trans.*, no. L, pp. 4657–4663, 2006.

[27] Y. Gao, J. Kuncheria, P. A. Yap, and R. J. Puddephatt, “An efficient binuclear catalyst for decomposition of formic acid,” *ChemComm*, pp. 2365–2366, 1998.

[28] T. C. Johnson, D. J. Morris, and M. Wills, “Hydrogen generation from formic acid and alcohols using homogeneous catalysts,” *Chem. Soc. Rev.*, vol. 39, no. 1, pp. 81–88, 2010.

[29] Ö. Metin, X. Sun, and S. Sun, “Monodisperse gold–palladium alloy nanoparticles and their composition-controlled catalysis in formic acid dehydrogenation under mild conditions,” *Nanoscale*, vol. 5, no. 3, pp. 910–912, 2013.

[30] Z.-L. Wang, J.-M. Yan, H.-L. Wang, Y. Ping, and Q. Jiang, “Au@Pd core–shell nanoclusters growing on nitrogen-doped mildly reduced graphene oxide with enhanced catalytic performance for hydrogen generation from formic acid,” *J. Mater. Chem. A*, vol. 1, no. 41, p. 12721, 2013.

[31] Q.-L. Zhu, N. Tsumori, and Q. Xu, “Sodium hydroxide-assisted growth of uniform Pd nanoparticles on nanoporous carbon MSC-30 for efficient and complete dehydrogenation of formic acid under ambient conditions,” *Chem. Sci.*, vol. 5, no. 1, pp. 195–199, 2014.

[32] M. Yadav and Q. Xu, “Liquid-phase chemical hydrogen storage materials,” *Energy Environ. Sci.*, vol. 5, no. 12, p. 9698, 2012.

[33] X. Zhou, Y. Huang, W. Xing, C. Liu, J. Liao, and T. Lu, “High-quality hydrogen from the catalyzed decomposition of formic acid by Pd–Au/C and Pd–Ag/C,” *Chem. Commun.*, no. 30, p. 3540, 2008.

[34] Q. Y. Bi, X. L. Du, Y. M. Liu, Y. Cao, H. Y. He, and K. N. Fan, “Efficient subnanometric gold-catalyzed hydrogen generation via formic acid decomposition under ambient conditions,” *J. Am. Chem. Soc.*, vol. 134, no. 21, pp. 8926–8933, 2012.

[35] Y. Noto, K. Fukuda, T. Onishi, and K. Tamaru, “Mechanism of formic acid decomposition over dehydrogenation catalysts,” *Trans. Faraday Soc.*, vol. 63, pp. 3081–3087, 1967.

[36] T. Fukuda, K.; Noto, Y.; Onishi, “Mechanism of Dehydration Decomposition of Formic Acid over Alumina and Silica,” *Trans. Faraday Soc.*, pp. 3072–3080, 1967.

[37] K. Noto, Y.; Fukuda, K.; Onishi, T.; Tamaru, “Dynamic Treatment of Chemisorbed Species by Means of,” *Trans. Faraday Soc.*, pp. 2300–2308, 1967.

[38] W. Jorgensen and R. J. Madix, “Active Oxygen on Group VIII Metals: Activation of Formic Acid and Formaldehyde on Pd(100),” *J. Am. Chem. Soc.*, vol. 110, no. 18, pp. 397–400, 1988.

[39] W. Erley and D. Sander, “The adsorption and decomposition of formic acid on Ni(111): The identification of formic anhydride by vibrational spectroscopy,” *J. Vac. Sci. Technol. A Vacuum, Surfaces, Film.*, vol. 7, no. 3, pp. 2238–2244, 1989.

[40] J. E. Crowell, J. G. Chen, and J. T. Yates, “A vibrational study of the adsorption and decomposition of formic acid and surface formate on Al(111),” *J. Chem. Phys.*, vol. 85, no. 5, p. 3111, 1986.

[41] M. D. Weisel, J. G. Chen, F. M. Hoffmann, Y. - K. Sun, and W. H. Weinberg, “A Fourier transform- infrared reflection absorption spectroscopy study of the formation and decomposition of chemisorbed formate on clean and potassium-modified Ru(001),” *J. Chem. Phys.*, vol. 97, no. 12, pp. 9396–9411, 1992.

[42] M. R. Columbia, A. M. Crabtree, and P. A. Thiel, “The temperature and coverage dependences of adsorbed formic acid and its conversion to formate on platinum(111),” *J. Am. Chem. Soc.*, vol. 114, no. 4, pp. 1231–1237, 1992.

[43] M. Bowker, E. Rowbotham, F. M. Leibsle, and S. Haq, “The adsorption and decomposition of formic acid on Cu {110},” *Surf. Sci.*, vol. 349, pp. 97–110, 1996.

[44] M. Bowker, S. Haq, R. Holroyd, P. M. Parlett, and S. Poulston, “Spectroscopic and Kinetic Studies of Formic Acid Adsorption on Cu(110),” *J. Chem. Soc.; Faraday Trans*, vol. 92, no. 23, pp. 4683–4686, 1996.

[45] N. Aas, Y. Li, and M. Bowker, “The adsorption and decomposition of formic acid on Cu(110),” *Surf. Sci.*, vol. 349, pp. 97–110, 1996.

[46] G. J. Millar, C. H. Rochester, and K. C. Waugh, “An FTIR Study of the Adsorption of Formic Acid and Formaldehyde on Potassium-Promoted Cu/SiO2 Catalysts,” *Journal of Catalysis*, vol. 155, no. 1. pp. 52–58, 1995.

[47] C. Xu and D. W. Goodman, “Adsorption and Reaction of Formic Acid on the Mo (110) and O/Mo (110) Surfaces,” *J. Phys. Chem.*, vol. 100, pp. 1753–1760, 1996.

[48] R. Larsen, S. Ha, J. Zakzeski, and R. I. Masel, “Unusually active palladium-based catalysts for the electrooxidation of formic acid,” *J. Power Sources*, vol. 157, pp. 78–84, 2006.

[49] S. Zhang, Ö. Metin, D. Su, and S. Sun, “Monodisperse AgPd Alloy Nanoparticles and Their Superior Catalysis for the Dehydrogenation of Formic Acid,” *Angew. Chemie Int. Ed.*, vol. 52, no. 13, pp. 3681–3684, 2013.

[50] M. Yurderi, A. Bulut, M. Zahmakiran, and M. Kaya, “Carbon supported trimetallic PdNiAg nanoparticles as highly active , selective and reusable catalyst in the formic acid decomposition,” *"Applied Catal. B, Environ.*, vol. 160–161, pp. 514–524, 2014.

[51] S. Li, Y. Ping, J.-M. Yan, H.-L. Wang, M. Wu, and Q. Jiang, “Facile synthesis of AgAuPd/graphene with high performance for hydrogen generation from formic acid,” *J. Mater. Chem. A*, vol. 3, no. 28, pp. 14535–14538, 2015.

[52] Y. Huang, J. Xu, X. Ma, Y. Huang, Q. Li, and H. Qiu, “An effective low Pd-loading catalyst for hydrogen generation from formic acid,” *Int. J. Hydrogen Energy*, pp. 4–11, 2017.

[53] J. Rasko, J. Ã. Kiss, and T. Kecske, “New reaction route of HCOOH catalytic decomposition,” *Vacuum*, vol. 80, pp. 64–68, 2005.

[54] S. Akbayrak, Y. Tonbul, and S. Ozkar, “Nanoceria supported palladium(0) nanoparticles: Superb catalyst in dehydrogenation of formic acid at room temperature,” *Appl. Catal. B Environ.*, vol. 206, pp. 384–392, 2017.

[55] G. C. Cabilla, A. L. Bonivardi, and M. A. Baltanás, “Infrared study of the adsorption of formic acid on clean and Ca-promoted Pd/SiO2 catalysts,” *Appl. Catal. A Gen.*, vol. 255, no. 2, pp. 181–195, 2003.

[56] Q. Yadav M; Singh, A. K.; Xu, “Palladium silica nanosphere-catalyzed decomposition of formic acid for chemical hydrogen storage,” *J. Mater. Chem.*, vol. 22, p. 19146, 2012.

[57] Y. Karatas, A. Bulut, M. Yurderi, I. E. Ertas, O. Alal, M. Gulcan, M. Celebi, H. Kivrak, M. Kaya, and M. Zahmakiran, “PdAu-MnOx Nanoparticles Supported on Amine-Functionalized SiO2 for the Room Temperature Dehydrogenation of formic acid in the absence of additives,” *"Applied Catal. B, Environ.*, vol. 180, no. January, pp. 586–595, 2016.

[58] K. Mandal, D. Bhattacharjee, and S. Dasgupta, “Synthesis of nanoporous PdAg nanoalloy for hydrogen generation from formic acid at room temperature,” *Int. J. Hydrogen Energy*, vol. 40, no. 14, pp. 4786–4793, 2015.

[59] Z.-L. Wang, J.-M. Yan, Y. Ping, H.-L. Wang, W.-T. Zheng, and Q. Jiang, “An Efficient CoAuPd/C Catalyst for Hydrogen Generation from Formic Acid at Room Temperature,” *Angew. Chemie Int. Ed.*, vol. 52, no. 16, pp. 4406–4409, 2013.

[60] M. Yurderi, A. Bulut, N. Caner, M. Celebi, M. Kaya, and M. Zahmakiran, “Amine grafted silica supported CrAuPd alloy nanoparticles: superb heterogeneous catalysts for the room temperature dehydrogenation of formic acid,” *Chem. Commun.*, vol. 51, no. 57, pp. 11417–11420, 2015.

[61] A. Ruban, B. Hammer, P. Stoltze, and H. L. Skriver, “Surface electronic structure and reactivity of transition and noble metals,” *J. Mol. Catal. A Chem.*, vol. 115, pp. 421–429, 1997.

[62] Y. Ding, W. Sun, W. Yang, and Q. Li, “Formic acid as the in-situ hydrogen source for catalytic reduction of nitrate in water by PdAg alloy nanoparticles supported on amine-functionalized SiO2,” *Appl. Catal. B Environ.*, vol. 203, pp. 372–380, 2017.

[63] M. Bernard, A. H. Goff, B. V. Thi, C. Physique, U. Pierre, and S. C. De Torresi, “Electrochromic Reactions in Manganese Oxides,” *J. Electrochem. Soc.*, vol. 140, no. 11, pp. 3065–3070, 1993.

[64] S. Wang, N. Li, R. Zhou, L. Jin, G. Hu, J. Lu, and M. Luo, “Chemical Comparing the CO oxidation activity of free PdO and Pd 2+ ions over PdO-CeO2/SiO2 catalyst,” *J. Mol. Catal. A*, vol. 375, pp. 53–58, 2013.

[65] Z. Zhao, J. Elwood, and M. A. Carpenter, “Phonon Anharmonicity of PdO Studied by Raman Spectrometry,” *J. Phys. Chem. C*, vol. 119, pp. 23094–23102, 2015.

[66] I. Martina, R. Wiesinger, and M. Schreiner, “Micro-Raman Characterization of Silver Corrosion Products : Instrumental Set Up and Reference,” vol. 9, pp. 1–8, 2012.

[67] S. Sukhishvili, “Effect of Oxidation on Surface-Enhanced Raman Scattering Activity of Silver Nanoparticles: A Quantitative Correlation,” *Anal. Chem.*, vol. 83, pp. 5873–5880, 2011.

[68] J. Zuo and C. Xu, “Raman Spectra of Nanophase Cr203,” *J. raman Spectrosc.*, vol. 27, pp. 921–923, 1996.

[69] C. Moisii, E. W. Deguns, A. Lita, S. D. Callahan, L. J. Van De Burgt, D. Magana, and A. E. Stiegman, “Coordination Environment and Vibrational Spectroscopy of Cr (VI) Sites Supported on Amorphous Silica,” *Chem. Matter.*, vol. 18, no. Vi, pp. 3965–3975, 2006.

[70] E. Groppo, A. Damin, F. Bonino, A. Zecchina, S. Bordiga, and C. Lamberti, “New Strategies in the Raman Study of the Cr / SiO 2 Phillips Catalyst : Observation of Molecular Adducts on Cr (II) Sites,” *Chem. Matter.*, vol. 17, pp. 2019–2027, 2005.

[71] A. V. Naumkin, A. Kraut-Vass, S. W. Gaarenstroom, and C. J. Powell, “NIST X-ray Photoelectron Spectroscopy Database,” 2012. [Online]. Available: https://srdata.nist.gov/xps/Default.aspx.

[72] G. Di Castro, V., & Polzonetti, “XPS study of MnO oxidation,” *J. Electron Spectros. Relat. Phenomena*, vol. 48, no. 1, pp. 117–123, 1989.

[73] C. H. F. Blair, D. S., Rogers Jr, J. W., & Peden, “Potassium-assisted, facile oxidation of Si3N4 thin films,” *J. Appl. Phys.*, vol. 67, no. 4, pp. 2066–2073, 1990.

[74] N. Gaarenstroom, S. W., & Winograd, “Initial and final state effects in the ESCA spectra of cadmium and silver oxides,” *J. Chem. Phys.*, vol. 67, no. 8, pp. 3500–3506, 1977.

[75] X. I. Inc, “Fundamental XPS Data from Pure Elements, Pure Oxides, and Chemical Compounds,” *1999*. [Online]. Available: http://www.xpsdata.com/.

[76] V. Y. Young, R. A. Gibbs, N. Winograd, and A. Si, “X-ray photoemission studies of atom implanted matrices :Cu, Ag, and Au in SiO2,” *J. Chem. Phys.*, vol. 70, no. 12, p. 5714, 1979.

[77] M. D. Tura, J. M., Regull, P., Victori, L., & De Castellar, “XPS and IR (ATR) analysis of Pd oxide films obtained by electrochemical methods,” *Surf. interface Anal.*, vol. 11, no. 8, pp. 447–449, 1988.

[78] J. K. Wilmshurst, “Vibrational Assignment in Monomeric Formic Acid,” *J. Chem. Phys.*, vol. 25, no. 3, pp. 478–480, 1956.

[79] Y. Mikawa, R. J. Jakobsen, and J. W. Brasch, “Infrared Evidence of Polymorphism in Formic Acid Crystals,” *J. Chem. Phys.*, vol. 45, p. 4750, 1966.

[80] G. Rubasinghege, S. Ogden, J. Baltrusaitis, and V. H. Grassian, "Heterogeneous Uptake and Adsorption of Gas-Phase Formic Acid on Oxide and Clay Particle Surfaces: The Roles of Surface Hydroxyl Groups and Adsorbed Water in Formic Acid Adsorption and the Impact of Formic Acid Adsorption on Water Uptake," 2013.

[81] National Institute of standards and technology, "NIST Standard Reference Database Number 69."[Online]. Available: http://webbook.nist.gov/chemistry/.

[82] J. Lundell, M. Pettersson, L. Khriachtchev, and E. M. S. Mac, "Vibrational spectroscopy of cis - and trans -formic acid in solid argon," vol. 219, pp. 70–80, 2003.

[83] J. P. Durand, S. D. Senanayake, S. L. Suib, and D. R. Mullins, "Reaction of formic acid over amorphous manganese oxide catalytic systems: An in situ study," *J. Phys. Chem. C*, vol. 114, no. 47, pp. 20000–20006, 2010.

[84] J. Raskó, T. Kecskés, and J. Kiss, "Formaldehyde formation in the interaction of HCOOH with Pt supported on TiO2," *J. Catal.*, vol. 224, no. 2, pp. 261–268, 2004.

[85] P. Rotzinger, J. M. Kesselman-truttmann, S. J. Hug, V. Shklover, and M. Gra, "Structure and Vibrational Spectrum of Formate and Acetate Adsorbed from Aqueous Solution onto the TiO2 Rutile (110) Surface Franc," no. 110, pp. 5004–5017, 2004.

[86] G. Y. Popova, Y. A. Chesalov, E. M. Sadovskaya, and T. V. Andrushkevich, "Effect of water on decomposition of formic acid over V-Ti oxide catalyst: Kinetic and in situ FTIR study," *J. Mol. Catal. A Chem.*, vol. 357, pp. 148–153, 2012.

[87] T. Zheng, D. Stacchiola, D. K. Saldin, J. James, D. S. Sholl, and W. T. Tysoe, "The structure of formate species on Pd (1 1 1) calculated by density functional theory and determined using low energy electron diffraction," vol. 574, pp. 166–174, 2005.

[88] J. Scaranto and M. Mavrikakis, "Density functional theory studies of HCOOH decomposition on Pd(111)," *Surf. Sci.*, vol. 650, pp. 111–120, 2016.

[89] S.-Y. Vannice, Albert M.; Wang, "Determination of IR Extinction Coefficients for Linear- and Bridged-Bonded CO on Supported Palladium," no. 85, pp. 2543–2546, 1981.

[90] K. Bechoux, O. Marie, M. Daturi, G. Delahay, C. Petitto, S. Rousseau, and G. Blanchard, "Infrared evidence of room temperature dissociative adsorption of carbon monoxide over Ag/Al2O3," *Catal. Today*, vol. 197, no. 1, pp. 155–161, 2012.

[91] Z. Qu, W. Huang, S. Zhou, H. Zheng, X. Liu, and M. Cheng, "Enhancement of the catalytic performance of supported-metal catalysts by pretreatment of the support," *J. Catal.*, vol. 234, pp. 33–36, 2005.

[92] Z. Qu, M. Cheng, X. Dong, and X. Bao, "CO selective oxidation in H2 -rich gas over Ag nanoparticles — effect of oxygen treatment temperature on the activity of silver particles mechanically mixed with SiO 2," *Catal. Today*, vol. 95, pp. 247–255, 2004.

[93] Ø. Espelid and K. J. Børve, "Theoretical Analysis of CO Adsorption on the Reduced Cr / Silica System," *J. Catal.*, vol. 205, pp. 177–190, 2002.

[94] M. Pykavy, V. Staemmler, O. Seiferth, and H. Freund, “Adsorption of CO on Cr2O3 (0001),” *Surf. Sci*.,vol. 479, pp. 11–25, 2001.

[95] A. C. Pavao, B. L. Hammond, M. M. Soto, W. A. Lester, and C. A. Taft, “Theoretical study of the CO interaction with the Cr (110) surface,” *Surf. Sci*., vol. 323, pp. 340–344, 1995.

[96] A. A. Davydov, *Infrared Spectroscopy of Adsorbed Species on the Surface of Transition Metal Oxides*. 1990.